Department of Precision and Microsystems Engineering

The Impact of the Engulfment Effect on the Auxeticity of Helical Auxetic Yarns

Ziqi Lyu

Report no	:	2024.071
Coach	:	P. (Pierre) Roberjot MEng
Professor	:	Prof.dr.ir. J.L. (Just) Herder
Specialisation	:	Mechatronic System Design (MSD)
Type of report	:	Master's Thesis
Date	:	13 August 2024

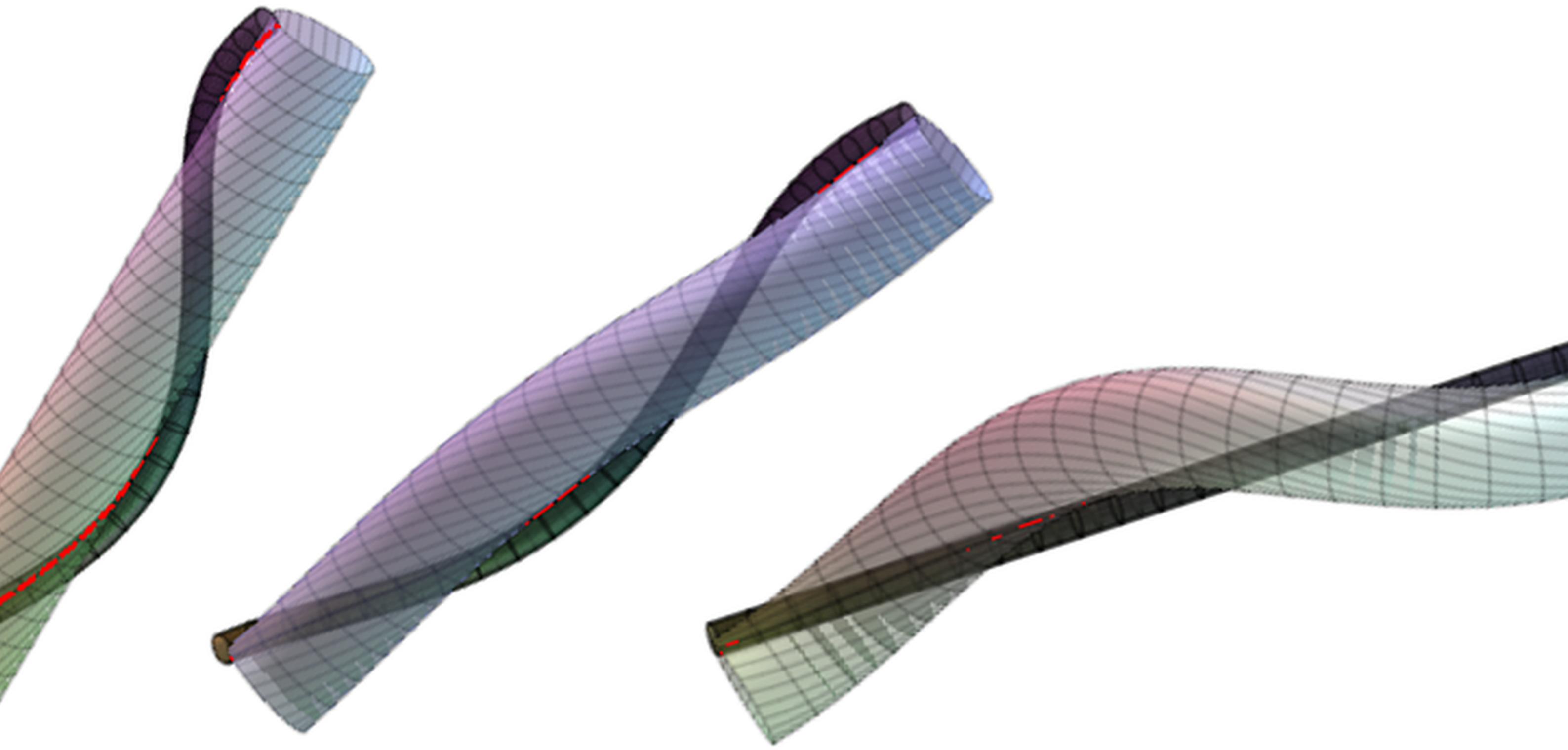

Delft University of Technology

Precision and Microsystems Engineering

Challenge the future

The Impact of the Engulfment Effect on the Auxeticity of Helical Auxetic Yarns

by

Ziqi Lyu

to obtain the degree of Master of Science
at the Delft University of Technology,
to be defended publicly on Friday August 30, 2024 at 11:00 AM.

Student number:	5705169	
Project duration:	September 1, 2023 – August 30, 2024	
Thesis committee:	Prof.dr.ir. J.L. (Just) Herder,	TU Delft, supervisor
	Dr. A. (Andres) Hunt,	TU Delft
	Dr. J. (Jovana) Jovanova,	TU Delft

This thesis is confidential and cannot be made public until December 31, 2024.

Cover: Representation of the stretching process of Helical Auxetic Yarns

An electronic version of this thesis is available at `http://repository.tudelft.nl/`.

TU Delft

Summary

Auxetic materials are a unique class of materials characterized by a negative Poisson's ratio, meaning they expand laterally when stretched longitudinally. This distinctive behavior offers advantages such as enhanced resistance to indentation, improved energy absorption, and increased fracture toughness. These properties make auxetic materials ideal for use in fields like soft robotics, biomedical devices, and advanced textiles.

Helical Auxetic Yarns (HAYs) are a novel auxetic structure where a stiffer fiber helically wraps around a more compliant core fiber. This design leads to significant lateral expansion under axial strain, making HAYs suitable for applications requiring flexibility and durability, such as healthcare, filtration, and textiles. Factors like the initial wrap angle, diameter ratio, and the Poisson's ratios of the fibers critically influence the auxetic behavior of HAYs.

This work investigates the impact of the engulfment effect on the auxetic behavior of HAYs by combining theoretical modeling, numerical simulations. It reveals that geometric and material parameters such as diameter ratio, Young's modulus, and wrap angle play crucial roles in determining auxeticity. The study identifies that while a higher diameter ratio enhances the auxetic effect, the engulfment effect—where the wrap fiber indents the core—can diminish the auxetic response under certain conditions. Strategic recommendations are provided for optimizing HAY design, such as balancing these parameters to achieve a stable and pronounced auxetic effect while minimizing the engulfment phenomenon. This research contributes valuable insights to the field of auxetic materials and paves the way for future applications of HAYs in various industries.

Contents

Nomenclature

Abbreviations

Abbreviation	Definition
HAY	Helical Auxetic Yarns
NPR	Negative Poisson's Ratio
PR	Poisson's Ratio
SW	Stiffer Wrap Fiber
CC	Compliant Core Fiber

Symbols

Symbol	Definition	Unit
D_{SW}	Diameter of Stiffer Wrap Fiber	$[mm]$
D_C	Diameter of Compliant Core Fiber at any time	$[mm]$
D_{CI}	Diameter of Compliant Core Fiber at Initial State	$[mm]$
D_{CT}	Diameter of Compliant Core Fiber at Twisted State	$[mm]$
D_{CF}	Diameter of Compliant Core Fiber at Final State	$[mm]$
D	Effective Diameter of HAYs at any time	$[mm]$
D_1	Effective Diameter of Stiffer Wrap Fiber Side	$[mm]$
D_2	Effective Diameter of Compliant Core Fiber Side	$[mm]$
L_{SW}	Length of Stiffer Wrap Fiber	$[mm]$
L_C	Length of Compliant Core Fiber at any time	$[mm]$
L_{CI}	Length of Compliant Core Fiber at Initial State	$[mm]$
L_{CF}	Length of Compliant Core Fiber at Final State	$[mm]$
L_S	Length of HAYs at any time	$[mm]$
L_{SI}	Length of HAYs at Initial State	$[mm]$
L_{SF}	Length of HAYs at Final State	$[mm]$
d_{SW}	Distance between the neutral lines of Stiffer Wrap Fiber and HAYs	$[mm]$
d_{CC}	Distance between the neutral lines of Compliant Core Fiber and HAYs	$[mm]$
E_{SW}	Young's Modulus of Stiffer Wrap Fiber	$[MPa]$
R	Radius of 3D Helix Equation	
n	Number of Pitches in HAYs	
$\tilde{r}_{SW}(t)$	Helix function of neutral line of Stiffer Wrap Fiber	
s	Arc length	
$\tilde{t}(t)$	Tangent Vector of Helix Function	
$\tilde{n}(t)$	Tangent Vector of $\tilde{t}(t)$	
$\tilde{b}(t)$	Vector orthogonal to Tangent Vector of Helix Function	
$S(t, u)$	Surface function of HAYs	
P	Pitch of HAYs	
$r_{contact(t)}$	Equation of Contact Line	
θ	Wrap Angle of Stiffer Wrap Fiber at any time	[°]
θ_I	Wrap Angle of Stiffer Wrap Fiber at Initial State	[°]
θ_T	Wrap Angle of Stiffer Wrap Fiber at Twisted State	[°]
θ_F	Wrap Angle of Stiffer Wrap Fiber at Final State	[°]
β	Wrap Angle of Compliant Core Fiber at any time	[°]

Symbol	Definition	Unit
β_T	Wrap Angle of Compliant Core Fiber at Twisted State	[°]
β_F	Wrap Angle of Compliant Core Fiber at Final State	[°]
ν_{SW}	Poisson's Ratio of Stiffer Wrap Fiber	
ν_{CC}	Poisson's Ratio of Compliant Core Fiber	
ϵ	Strain of HAYs	
ϵ_{max}	Maximum Strain of HAYs	
ϵ_C	Strain of Compliant Core Fiber	

1

Introduction

Auxetic metamaterials[1] are a relatively new class of functional materials characterized by a negative Poisson's ratio, meaning they expand laterally when stretched longitudinally[2]. Three well-established basic structures can explain these mechanisms (Fig. 1.1): re-entrant structures, chiral structures, and rotating rigid structures[3, 4]. These materials offer many benefits, including higher indentation resistance, shear resistance, energy absorption, hardness, and fracture toughness[5, 6, 7]. Nowadays, auxetic materials have been utilized in many innovative applications such as soft robotics[8], bio-medicine[9], and soft electronics[10].

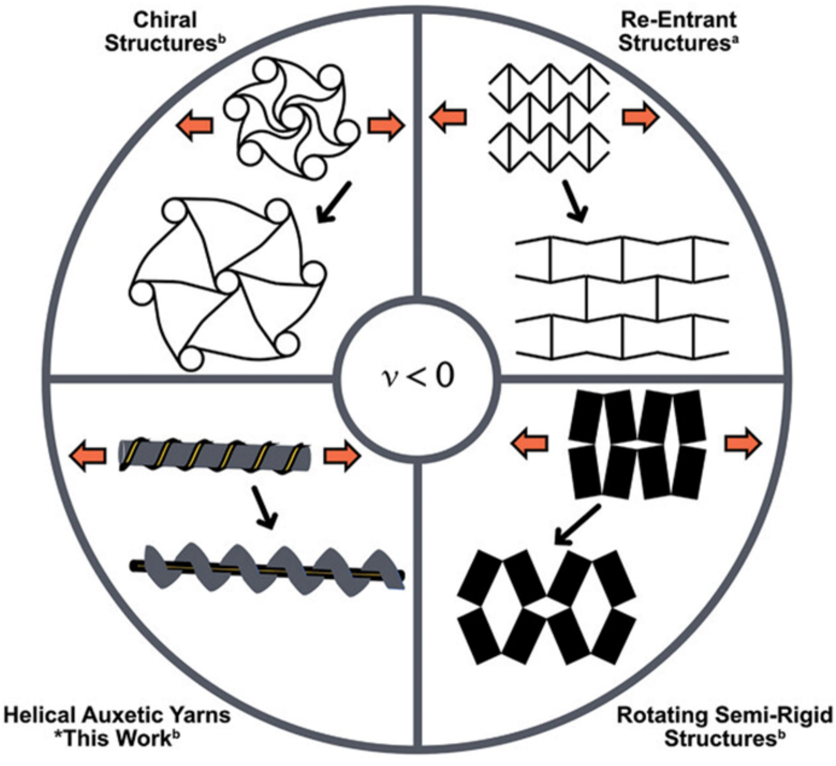

Figure 1.1: Different auxetic mechanical structures[11]

Hook et al.[12] proposed a novel geometry and composite for auxetic behavior in the form of a helically wrapped yarn, which can achieve a significant negative Poisson's ratio both independently and within a textile. This structure is known as helical auxetic yarn (HAY). These yarns are categorized based on the number of fibers, denoted as n-plys HAYs, such as 2-plys and 4-plys, as shown in Fig. 1.2. And in this work, HAYs will refer to 2-plys HAYs(Fig. 1.2A). HAYs consists of two conventional fibers, where a relatively stiffer and thinner fiber is helically wrapped around a more compliant and thicker core fiber, as illustrated in Fig. 2.1. When longitudinal strain is applied, the difference in the modulus of elasticity and diameters of the two fibers causes the compliant core to displace laterally due to the stiffer wrap fiber, resulting in an overall lateral expansion of the yarn's maximal width. By carefully selecting the fiber diameters, modulus, and the initial geometry of HAYs, a substantial negative Poisson's ratio can be achieved.

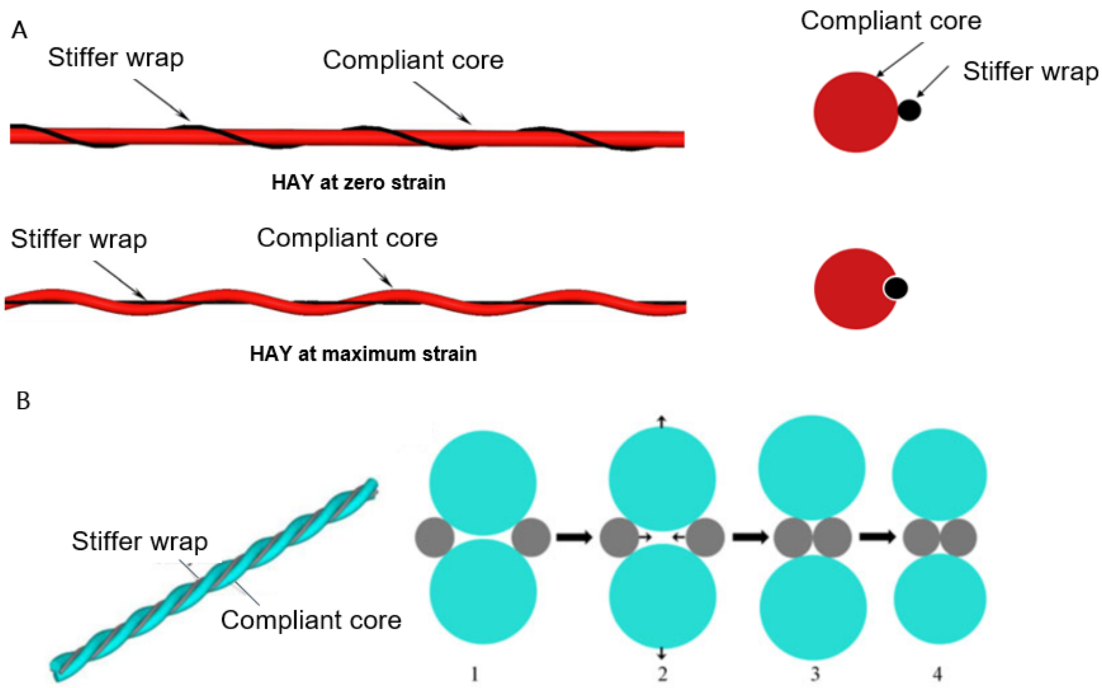

Figure 1.2: 2-plys(A)[13, 14] and 4-plys(B)[15] Helical Auxetic Yarns with their cross sections

HAYs have potential applications in filtration[14] and healthcare[16]. Since its invention, the basic structure and mechanics of HAYs have been extensively investigated both experimentally and theoretically[17, 18, 19, 13, 20]. Due to its diverse applications, ongoing research aims to improve its performance. Additionally, other types of auxetic fibers have been developed by researchers for textile applications[21, 22, 23]. Sloan et al.[13] identified that the initial wrap angle significantly impacts the auxetic behavior of HAYs, influencing both the degree and range of strain. They also noted that factors such as the diameter ratio between the wrap and core fibers and the inherent Poisson's ratio of the fibers play crucial roles. Their research focused on stiffer HAYs suitable for high-modulus applications, such as composites and blast mitigation. Wright et al.[24] explored the manufacturing and properties of various HAYs and fabrics with lower stiffness or tensile modulus, finding that their auxetic effects were practical for real-world applications. These materials were deemed suitable for healthcare uses like bandages and compression garments, as well as fashion. They found that HAYs were particularly effective in woven fabrics, with the produced plain weave fabric demonstrating an out-of-plane negative Poisson's ratio due to its thickening. Shanahan et al.[25] examined the auxetic behavior in fabric thickness, attributing it to the geometric impact of the woven structure and yarn modulus, highlighting the theoretical auxetic properties in the effective thickness of fabrics. Ge and Hu[15] introduced a novel auxetic plied yarn structure incorporating two different types of yarn components (Fig. 1.2(B)). This structure consists of two soft yarns and two stiff yarns, aiming to provide better control over the yarn's twist compared to traditional helical auxetic yarns, thereby enhancing twist regularity and overall stability of the auxetic yarn.

However, there is still a less clear phenomenon named engulfment effect happening. The configuration of a HAY requires the core to be more flexible than the wrap. If the core is both compliant and elastic, it performs two functions: enabling large lateral deformation when strain is applied and acting as a 'return spring' to recover its original position and reform the helix in the wrap once the load is removed. However, the compliance of the core can potentially introduce an undesirable mechanism within the HAYs. Under tension, the wrap may indent and embed itself into the surface of the core. Consequently, this interaction could reduce the negative Poisson's ratio and thus diminish the auxetic behavior of the HAYs. These interactions are illustrated in Fig. 1.3.

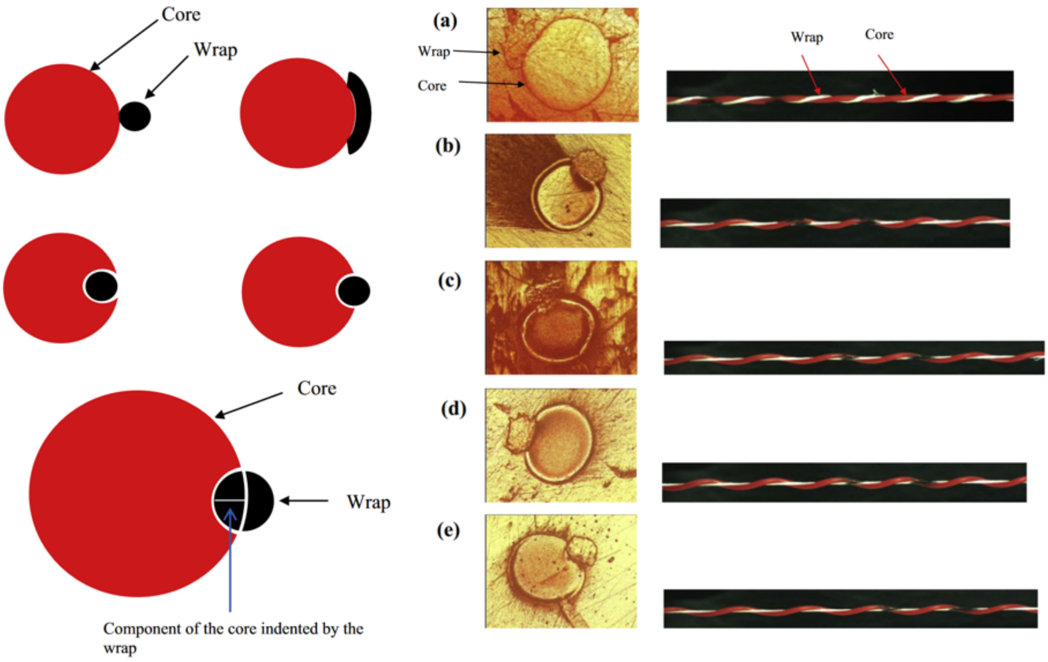

Figure 1.3: Possible cases(left) of engulfment effect and cross-sectional and external images(right)

This work develops an innovative theoretical model to investigate the auxetic behavior of Helical Auxetic Yarns (HAYs) by examining various parameters such as Young's modulus and diameter ratio. The model introduces a novel triangular approach that transitions the cross-sectional assumption from a circle to an ellipse, allowing for more accurate predictions of HAYs behavior from initial to final states. Additionally, a detailed helical 3D model of HAYs was derived using Maple, further refining the analysis. The finite element model for HAYs was established in Abaqus, and through numerical simulations, this work systematically explored the relationship between the initial wrapping angle, the diameter ratio of the fibers, and the resulting Poisson's ratio. This provided a comprehensive reference for future studies on the Negative Poisson's Ratio (NPR) effect in HAYs, contributing valuable insights for optimizing their design.

2

Methodology

2.1. Geometrical Description of the HAYs

2.1.1. Geometrical Model

A helical auxetic yarn (HAY) is constructed by combining two fibrous components in a double helix, as described by Hook et al.[12]. For optimal functionality, it is proposed that the components must have different modulus and diameters. The yarn geometry is first introduced: a low-modulus, initially straight core fiber is uniformly wrapped with a stiffer wrap component of a smaller diameter, as shown in Fig. 2.1(a). At zero strain, the compliant core and the stiffer wrap fibers are in uniform contact, with the core straight and the wrap helically wound with an internal helix diameter equal to the diameter of the core fiber. Upon the application of axial tensile strain(Fig. 2.1(b)), the wrap fiber straightens, displacing the core laterally and thus increasing the effective diameter of the system. At full strain, the geometry of the core and wrap fibers is reversed compared to the starting configuration. Fig. 2.1(c) shows the HAYs at maximum strain.

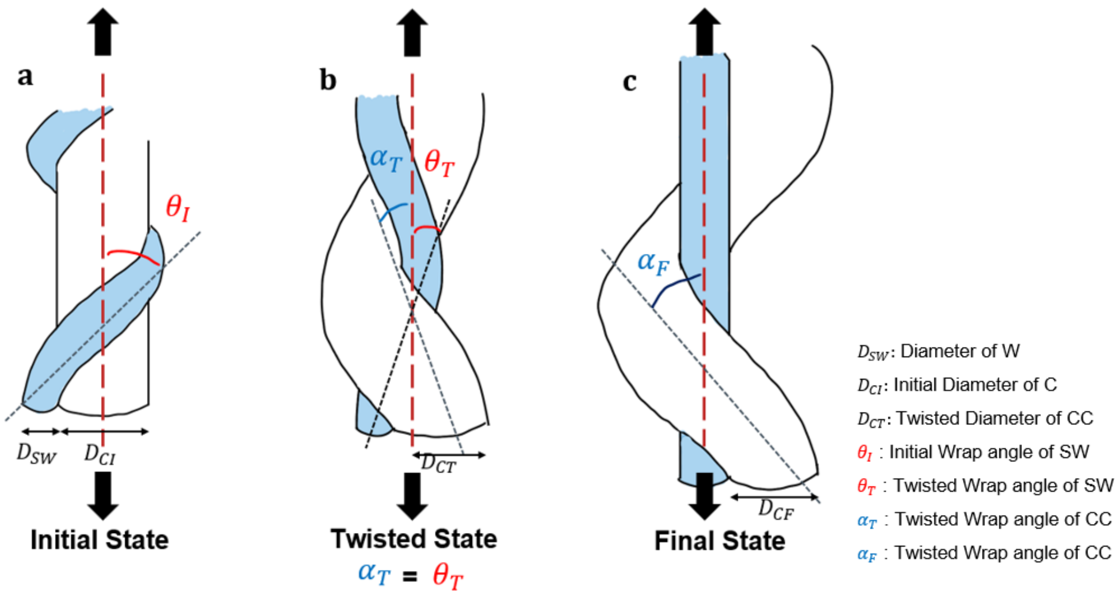

Figure 2.1: Three states of the HAYs, (a)the initial state, (b)the twisted state, (c)the final state

Fig. 2.2 defines the geometric parameters associated with HAYs having components of circular cross section. The initial diameters of the compliant core and stiffer wrap fibres can be defined as D_{CI} and D_{SW}, respectively. To predict the behavior of HAYs, we focused on the initial and final states. This

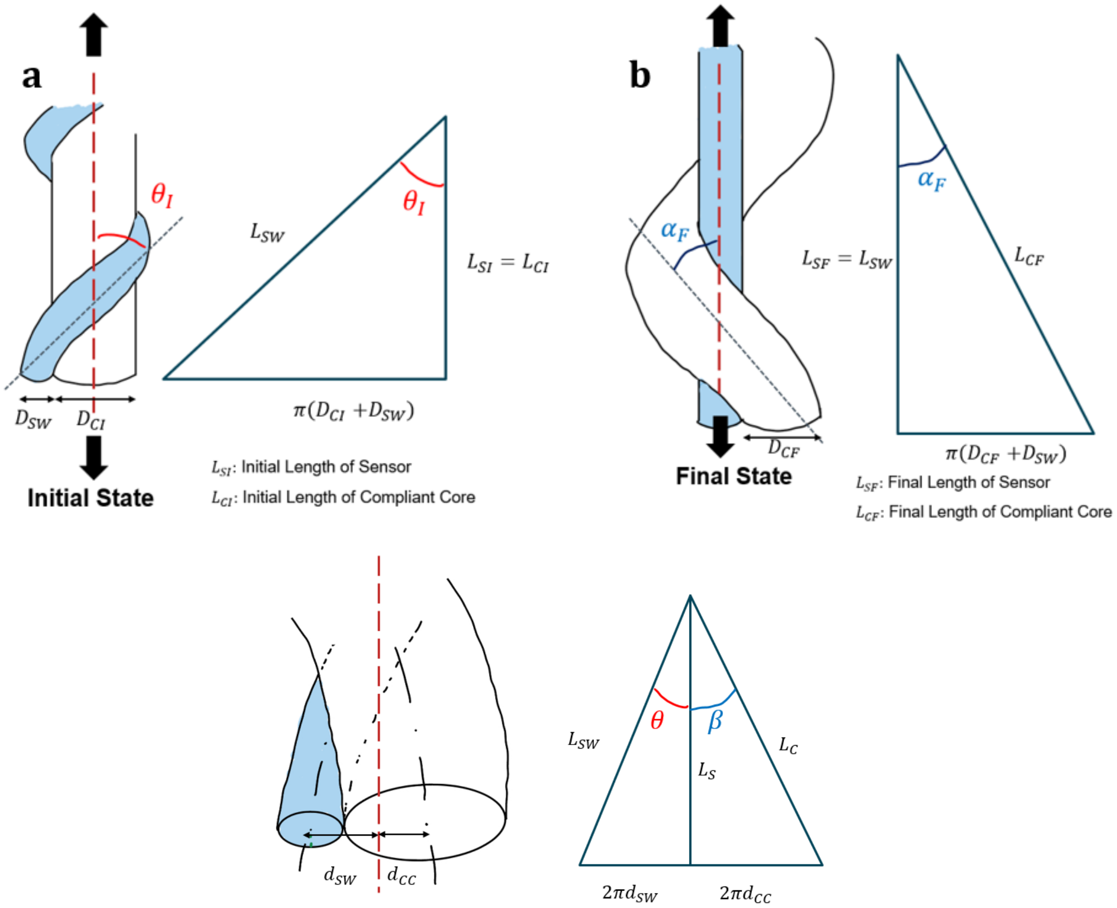

Figure 2.2: Geometrical representations of (a)initial and (b)final states; Triangular model with distance between neutral lines

approach allows us to make an initial prediction of the auxetic character at these well-defined points.

Assumptions:

- Both axial strain and radial strain of stiffer wrap fiber is zero.
- Two fibers always kept in contact and the interactive force was evenly distributed.
- One pitch of HAYs could be selected to represent the n-pitchs HAYs(means $n = 1$).

In the initial state, the stiffer wrap fiber of length L_{SW}, diameter D_{SW}, and Poisson's ratio $\nu_{SW} = 0.34$ is wrapped with an angle θ_I around the compliant core fiber of length L_{CI}, diameter D_{CI}, and Poisson's ratio ν_{CC} (here we will consider $\nu_{CC} = 0.45$). with triangular model, the length of stiffer wrap L_{SW} and the initial length of compliant core L_{CI} could be derived as

$$L_{\text{SW}} = \frac{\pi(D_{\text{CI}} + D_{\text{SW}})}{\sin(\theta_I)} \tag{2.1}$$

$$L_{\text{CI}} = L_{\text{SW}} \cdot \cos(\theta_I) \tag{2.2}$$

$$L_{\text{S}} = L_{\text{SW}} \cdot \cos(\theta) \tag{2.3}$$

The initial length of HAYs (no strain is applied) is defined by the length of compliant core fiber

$$L_{\text{SI}} = L_{\text{CI}} \tag{2.4}$$

In the final state, the stiffer wrap fiber replaces the core position and defines the final length of HAYs $L_{SF} = L_{SW}$. Then the final length of compliant core is

$$L_{\mathsf{CF}} = \sqrt{L_{\mathsf{SF}}^2 + \pi^2(D_{\mathsf{SW}} + D_{\mathsf{CF}})^2} \tag{2.5}$$

The angle θ goes from the initial angle θ_I at the initial length L_{SI} (when no strain is applied) to a final angle θ_F at the final length L_{SI}, meanwhile the angle α goes from the initial angle 0 to a final angle α_F. The evolution of the angle θ and angle α are known at every stage by the length of HAYs and given by the trigonometry formula:

$$\cos(\theta) = \frac{L_S}{L_{SW}} \tag{2.6}$$

$$\theta = \arccos\left(\frac{L_S}{L_{SW}}\right) \tag{2.7}$$

$$\cos(\alpha) = \frac{L_S}{L_C} \tag{2.8}$$

$$\alpha = \arccos\left(\frac{L_S}{L_C}\right) \tag{2.9}$$

We can define the strain applied on HAYs as:

$$\epsilon = \frac{L_{\mathsf{S}} - L_{\mathsf{SI}}}{L_{\mathsf{SI}}} = \frac{1}{\cos(\theta)} - 1 \tag{2.10}$$

$$\epsilon_{max} = \frac{L_{\mathsf{SF}} - L_{\mathsf{SI}}}{L_{\mathsf{SI}}} \tag{2.11}$$

And substitute length with strain, the formula of θ is

$$\theta = \arccos\left(1 + \epsilon\right)\cos\theta_I \tag{2.12}$$

In order to get parameters from every state, distances between neutral lines d_{SW} and d_{CC} are derived according to Fig. 2.2

$$d_{SW} = \frac{L_{SW}\sin(\theta)}{2\pi} \tag{2.13}$$

$$d_{CC} = \frac{D_{SW}}{2} + \frac{D_C}{2} - d_{SW} \tag{2.14}$$

The diameter of the compliant core fiber, dependant on the strain applied is reduced due to the Poisson's ratio. The general Poisson's equation, that is not limited to small strain, is the following:

$$\left(1 + \frac{\Delta L_C}{L_{CI}}\right)^{-\nu_{CC}} = 1 + \frac{\Delta D_C}{D_{CI}} \tag{2.15}$$

For small strain, the first order approximation yields to the "classical Poisson's equation":

$$D_C = (1 - \nu_{CC}\epsilon_C)D_{CI} \tag{2.16}$$

where ϵ_C is calculated from

$$\epsilon_C = \frac{L_C - L_{CI}}{L_{CI}} = \frac{\sqrt{(2\pi d_{CC})^2 + {L_S}^2} - L_{CI}}{L_{CI}} \tag{2.17}$$

The effective diameter of HAYs is defined by D is always the maximum between D_1 and D_2, and $D_I = 2D_{SW} + D_{CI}$. Fig. 2.3 shows the behavior of D related to D_1 and D_2, where

$$D_1 = D_{SW} + 2d_{SW}, \quad D_2 = D_C + 2d_{CC} \tag{2.18}$$

$$D = Max(D_1, D_2) \tag{2.19}$$

Consequently, with the maximum strain ϵ_{max}, the strain range is uniformly divided into 100 equal parts, resulting in 100 states throughout the process. By combining this with equations 2.14, 2.16, and 2.17, all the geometric parameters can be derived. And the Poisson's ratio could be calculated following the equation

$$PR = \frac{\frac{D - D_I}{D_I}}{\epsilon} \tag{2.20}$$

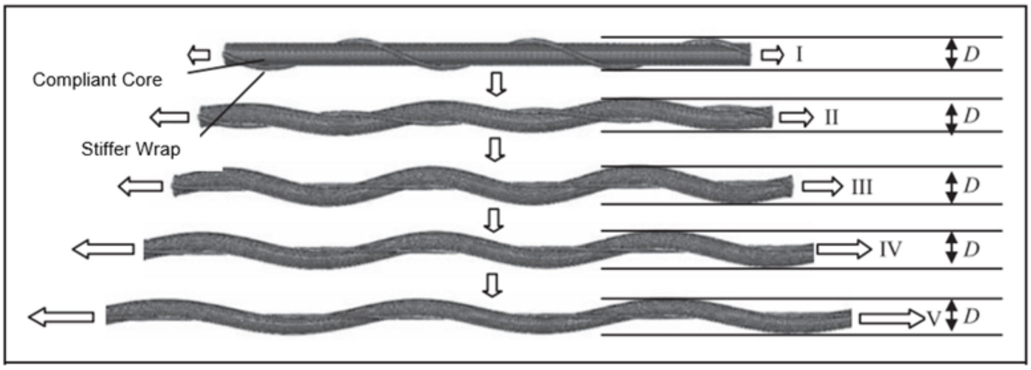

Figure 2.3: Effective Diameter D illustration

2.1.2. 3D Model in Maple

Based on the theoretical analysis of HAYs in the previous section, all the geometric parameters are now known. In this section, we aim to construct a three-dimensional model using these parameters. Maple is a powerful software tool well-suited for symbolic computation and mathematical modeling. All the work in this section was completed using Maple (Appendix A.2).

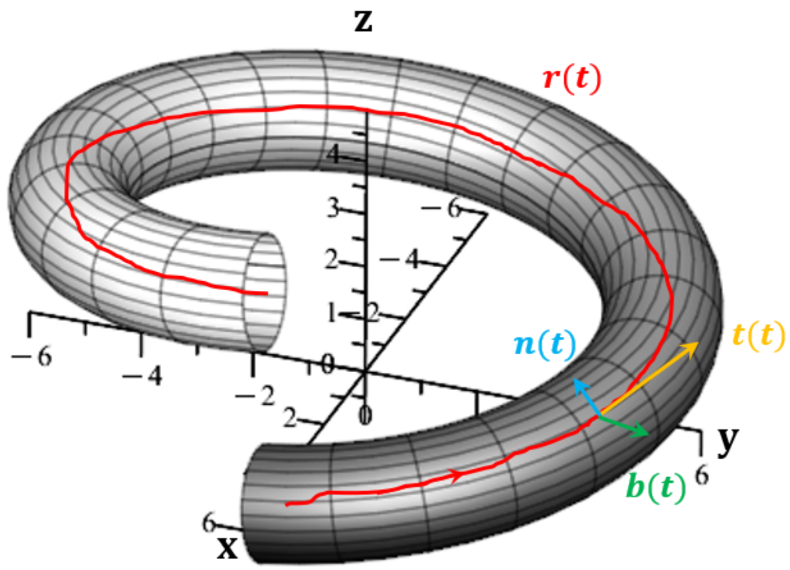

Figure 2.4: Helical 3D schematic figure

First, we assume that the shape of the neutral lines of both fibers approximates the Helix equation (where $n = 1$ and $P = L_S$):

$$\begin{cases} x(t) = R\cos(t) \\ y(t) = R\sin(t) \\ z(t) = \frac{nP}{2\pi}t \end{cases} \Rightarrow \quad r_{SW}(t) = \begin{cases} x(t) = d_{\mathsf{SW}}\cos(t) \\ y(t) = d_{\mathsf{SW}}\sin(t) \\ z(t) = \frac{nP}{2\pi}t \end{cases} \quad r_{CC}(t) = \begin{cases} x(t) = d_{\mathsf{CC}}\cos(t+\pi) \\ y(t) = d_{\mathsf{CC}}\sin(t+\pi) \\ z(t) = \frac{nP}{2\pi}t \end{cases} \tag{2.21}$$

Next, since the two fibers share similar equations, we can analyze the stiffer wrap fiber using its helix function of the neutral line $\vec{r}_{\mathsf{SW}}(t)$. The tangent vector can be obtained by differentiating:

$$\vec{t}(t) = \frac{d\vec{r}_{\mathsf{SW}}(t)}{dt} = \left(-d_{\mathsf{SW}}\sin t, d_{\mathsf{SW}}\cos t, \frac{nP}{2\pi}\right). \tag{2.22}$$

We note that this has a constant length $\sqrt{d_{\text{SW}}^2 + \left(\frac{nP}{2\pi}\right)^2}$. With a more general curve, this is not necessarily the case, and we would normalize this to unit length and switch to using the natural parameter $s =$ arc length. This time $ds/dt = \sqrt{d_{\text{SW}}^2 + \left(\frac{nP}{2\pi}\right)^2}$, and we can keep using t as long as we remember to normalize.

We obtain a local normal $\vec{n}(t)$ vector by differentiating the normalized tangent:

$$\vec{n}(t) = \frac{d}{dt}\left(\frac{\vec{t}(t)}{\|\vec{t}(t)\|}\right) = (-\cos t, -\sin t, 0)\,. \tag{2.23}$$

As the name suggests, this is orthogonal to the tangent vector (in the direction of change of the tangent). The third basis vector is the bi-normal:

$$\vec{b}(t) = \frac{1}{\|\vec{t}(t)\|}\left(\vec{t}(t) \times \vec{n}(t)\right) = \frac{1}{\sqrt{d_{\text{SW}}^2 + \left(\frac{nP}{2\pi}\right)^2}}\left(\frac{nP}{2\pi}\sin t, -\frac{nP}{2\pi}\cos t, d_{\text{SW}}\right). \tag{2.24}$$

This is, of course, orthogonal to both $\vec{t}$ and $\vec{n}$.

The key is that we get the desired surface by drawing (3D) circles with the axis direction determined by the direction of the curve, i.e., the tangent. Equivalently, we draw a circle of diameter d_{SW} in the plane spanned by $\vec{n}$ and $\vec{b}$. Hence, we get the entire surface S parameterized as:

$$S(t,u) = \vec{r}_{\text{SW}}(t) + \frac{d_{SW}}{2}\vec{n}(t)\cos u + \frac{d_{SW}}{2}\vec{b}(t)\sin u \tag{2.25}$$

with t ranging over many loop, and u ranging over the interval $[0, 2\pi]$. In terms of individual coordinates,

$$\begin{cases} x(t,u) = d_{\text{SW}}\cos(t) - \frac{d_{SW}}{2}\cos(t)\cos(u) + \frac{\frac{d_{SW}}{2}\left(\frac{nP}{2\pi}\right)\sin(t)\sin(u)}{\sqrt{(\frac{d_{SW}}{2})^2+\left(\frac{nP}{2\pi}\right)^2}} \\ y(t,u) = d_{\text{SW}}\sin(t) - \frac{d_{SW}}{2}\sin(t)\cos(u) + \frac{\frac{d_{SW}}{2}\left(\frac{nP}{2\pi}\right)\cos(t)\sin(u)}{\sqrt{(\frac{d_{SW}}{2})^2+\left(\frac{nP}{2\pi}\right)^2}} \\ z(t,u) = \frac{nP}{2\pi}t + \frac{(\frac{d_{SW}}{2})^2\sin(u)}{\sqrt{(\frac{d_{SW}}{2})^2+\left(\frac{nP}{2\pi}\right)^2}} \end{cases} \tag{2.26}$$

Finally, based on the results above, we could derive the helix equation of the contact line between two fibers, which is

$$r_{contact}(t) = \begin{cases} x(t) = (d_{\text{SW}} - \frac{D_{SW}}{2})\cos(t) \\ y(t) = (d_{\text{SW}} - \frac{D_{SW}}{2})\sin(t) \\ z(t) = \frac{nP}{2\pi}t \end{cases} \tag{2.27}$$

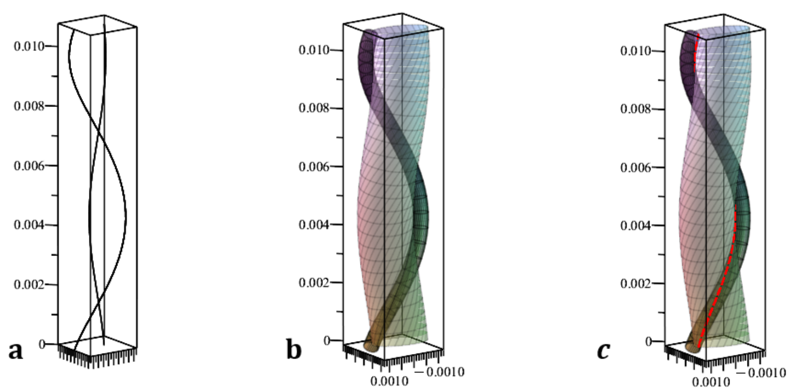

Figure 2.5: (a)Helix function of neutral lines, (b)with cross circles, (c)with contact line.

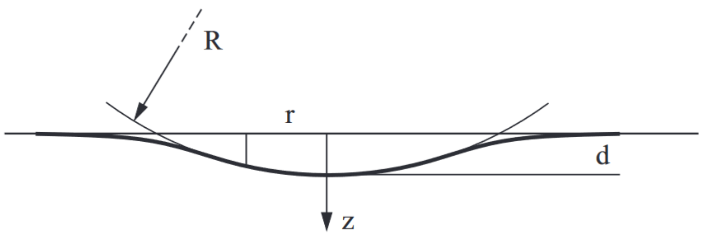

(a) A rigid sphere in contact with an elastic half-space

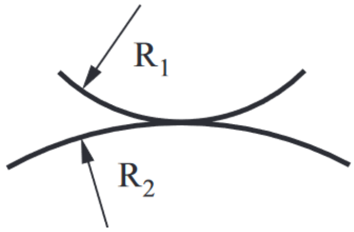

(b) Contact between two bodies with curved surfaces.

Figure 2.6: Illustrations of contact theory[26]

2.2. Description of Engulfment effect in HAYs

2.2.1. Hertz Contact Theory

Contact mechanics focuses on the study of how solids deform when they come into contact at one or several points. The study of elastic body contact is particularly useful for determining contact areas and depths of indentation in simple geometries. Currently, there are established solutions for a variety of technically significant shapes, including truncated cones, worn spheres, rough profiles, and hollow cylinders[26].

In Fig. 2.6a, a contact between a rigid sphere and an elastic half-space is shown schematically. The displacement of the points on the surface in the contact area between an originally even surface and a rigid sphere of radius R is equal to

$$u_z = d - \frac{r^2}{2R} \tag{2.28}$$

And it is assumed the pressure is exerted on a circle-shaped area with the radius a. It follows for the contact radius

$$a^2 = Rd \tag{2.29}$$

and for the maximum pressure

$$p_0 = \frac{2}{\pi} E^* \left(\frac{d}{R}\right)^{1/2} \tag{2.30}$$

Then we obtain a normal force of

$$F = \frac{4}{3} E^* R^{1/2} d^{3/2} \tag{2.31}$$

The results from Hertz's theory (2.28), (2.29) and (2.30) can also be used with few modifications in the following cases.

(A) If both bodies are elastic, then the following expression for E^* must be used:

$$\frac{1}{E^*} = \frac{1-\nu_1^2}{E_1} + \frac{1-\nu_2^2}{E_2} \tag{2.32}$$

Here, E_1 and E_2 are the modulus of elasticity and ν_1 and ν_2 the Poisson's ratios of both bodies.

(B) If two spheres with the radius R_1 andR_2 are in contact (Fig. 2.6b), then the equations (2.28), (2.29), and (2.30) are valid using the equivalent radius R :

$$\frac{1}{R} = \frac{1}{R_1} + \frac{1}{R_2} \tag{2.33}$$

2.2.2. Load analysis in HAYs

Considering the compressive force exerted on the contact line due to the stretching along the neutral axis of the stiffer wrap, we refer to the model proposed by S.Machida[27, 28], as illustrated in Fig. 2.7.

The estimation of such lateral pressure in a yarn has been based, in the past, on the assumption that the fibres as structural members do not possess either bending or torsional rigidity. Under this assumption,

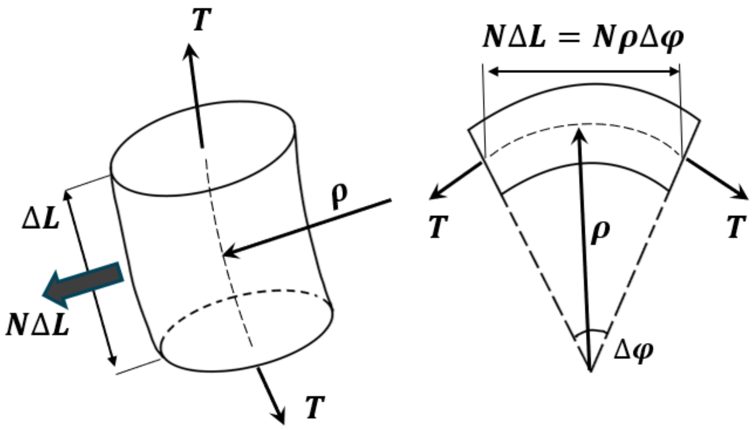

Figure 2.7: Equilibrium of force in an element of stiffer wrap fiber

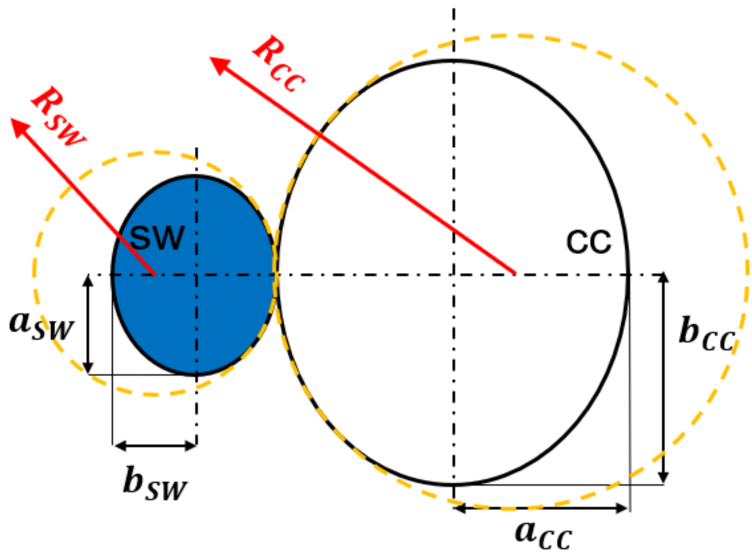

Figure 2.8: Cross section of HAYs at random state

the lateral force (linear density) on a fibre under tension, when bent against a curved surface of constant radius, is derived as:

$$N = \frac{T}{\rho} \tag{2.34}$$

where N is the lateral force per unit length, T is the tension in the stiffer wrap fibre, and ρ is the radius of curvature of the contact surface.

2.2.3. Contact Model in HAYs

Based on Hertz Contact theory, it is essential to understand the contact situation. To do this, we examine the cross section of HAYs at a random state, as shown in Fig. 2.8 The cross sections of both fibers will be ellipses but not perfect circles due to the effect of the wrap angle on each fiber. Assumption: consider the stiffer wrap fiber as elastic fiber but with extremely high Young's modulus while applying contact models.

Then, with known parameters, the major radius and the minor radius of each ellipse, a_{SW}, b_{SW}, a_{CC},

b_{CC}, could be derived as equations

$$ellipse_{SW}\begin{cases} a_{SW} = \frac{D_{SW}}{2} \\ b_{SW} = \frac{D_{SW}}{2\cos\theta} \end{cases} \quad ellipse_{CC}\begin{cases} a_{CC} = \frac{D_C}{2} \\ b_{CC} = \frac{D_C}{2\cos\alpha} \end{cases} \tag{2.35}$$

The contact between two elliptical cross-sections can be approximated as the contact between two circular surfaces, yellow dotted circle in Fig. 2.8. The approximate radius of the circles is the radius of curvature of each ellipse at the contact point. Given the parameters of the two ellipses, their respective radii of curvature can be determined using the following equations:

$$R_{\text{SW}} = \frac{(b_{\text{SW}})^2}{a_{\text{SW}}} \quad \text{and} \quad R_{\text{CC}} = \frac{(b_{\text{CC}})^2}{a_{\text{CC}}} \tag{2.36}$$

According to Hertz Contact Theory, the contact surface of HAYs conforms to the model of contact between two bodies with curved surfaces, as shown in Fig. 2.6b. Therefore, the effective radius R_{eff} is given by eq. 2.33 as

$$\frac{1}{R_{eff}} = \frac{1}{R_{SW}} + \frac{1}{R_{CC}} \tag{2.37}$$

When analyzing the existing contact models in comparison with the HAYs situation, two models exhibit similarities to the real case: Model 1 (Fig. 2.9a) and Model 2 (Fig. 2.9b). However, both models still have discrepancies when compared to the ideal scenario. Consequently, this work introduces Model 3 (Fig. 2.9c), which integrates and improves upon the advantages of the previous two models. Following paragraphs will discuss the models in detail.

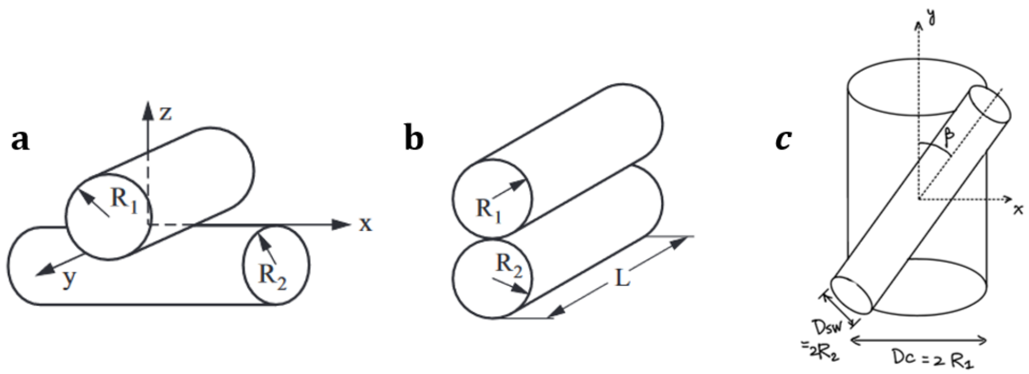

Figure 2.9: Three contact models: (a)Two crossed cylinders in contact, (b)Two cylinders in contact with parallel axes, (c)Two cylinders in contact with angle β

Model 1

If two elastic cylinders are in contact and lie on perpendicular axes with radius R_1 and R_2 (Fig. 2.9a), then the distance between the surfaces of both bodies at the moment of the first contact (still without deformation) is given by

$$h(x, y) = \frac{x^2}{2R_1} + \frac{y^2}{2R_2}. \tag{2.38}$$

This is exactly in accordance with a contact between an elastic half-space and a rigid body for ellipsoids with radius of curvature R_1 and R_2. Therefore, Hertz relations are valid if the effective radius

$$\tilde{R} = \sqrt{R_1 R_2}. \tag{2.39}$$

is used. Given the uniformly distributed compressive pressure N per unit length along the contact line from eq. 2.34 and the contact radius parameter a, the force F can be approximated as $F \approx N \cdot 2a$. Then combine eq. 2.29 and eq. 2.31, and substitute r with R_{eff}, we get

$$
\begin{aligned}
N \cdot 2a &= \frac{4}{3} E^* R^{\frac{1}{2}} d^{\frac{3}{2}} \\
\Rightarrow N \cdot 2\sqrt{Rd} &= \frac{4}{3} E^* R^{\frac{1}{2}} d^{\frac{3}{2}} \\
\Rightarrow d &= \frac{3}{2} \frac{N}{E^*}
\end{aligned} \tag{2.40}
$$

where d is the maximum engulfment displacement at the contact area.

Model 2

In the case of the contact between two cylinders with parallel axes (Fig. 2.9b), the force is linearly proportional to the penetration depth

$$F = \frac{\pi}{4} E^* L d \tag{2.41}$$

where $F = N \cdot L$. Then substitute the term in eq. 2.41, we could get

$$
\begin{aligned}
N \cdot L &= \frac{\pi}{4} E^* L d \\
\Rightarrow d &= \frac{4}{\pi} \frac{N}{E^*}
\end{aligned} \tag{2.42}
$$

Model 3

We assume that the contact plane is horizontal and $\beta = \theta + \alpha$. The distance between the surface of the first cylinder and this plane (at the first moment of contact) z_1 and the distance for the second cylinder z_2 are equal to

$$z_1 = \frac{x^2}{2R_1}, \quad z_2 = -\frac{(\cos(\beta)x - \sin(\beta)y)^2}{2R_2} \tag{2.43}$$

The distance between both surfaces is then

$$h = z_1 - z_2 = \frac{x^2}{2R_1} + \frac{(\cos(\beta)x - \sin(\beta)y)^2}{2R_2} \tag{2.44}$$

The principal curvatures are calculated as the eigenvalues of this quadratic form, using the equation,

$$\begin{vmatrix} \frac{\cos^2(\beta)}{R_2} + \frac{1}{R_1} - \kappa & -\frac{\cos(\beta)\sin(\beta)}{R_2} \\ -\frac{\cos(\beta)\sin(\beta)}{R_2} & \frac{\sin^2(\beta)}{R_2} - \kappa \end{vmatrix} = 0$$

to κ_1 and κ_2. Then the principal radius of curvature are accordingly ${R_{1,2}}' = \frac{1}{\kappa_{1,2}}$.

Based on eq. 2.39, the resulting Gaussian radius of curvature is

$$\tilde{R} = \sqrt{{R_1}'{R_2}'} \tag{2.45}$$

We assume the contact force per unit length works on a small contact distance δl, where $\delta l = D_{SW} \sin\beta$. Then with eq. 2.31. In this case, the relationship between the force and the penetration depth is

$$d = \left(\frac{3}{4} \frac{N \cdot d_l}{E^* \tilde{R}^{\frac{1}{2}}} \right)^{\frac{2}{3}} \tag{2.46}$$

And for all three models, E^* follows eq. 2.32.

2.3. Finite Element Analysis

The model of HAYs is constructed using Abaqus software. According to the theoretical model in Fig. 2.2, the parameters are applied to establish the finite element model of HAYs. Fig. 2.10 shows the 3D model of fiber HAYs. This model is built based on the actual parameters and consists of two parts: the 'stiffer wrap' and the 'compliant core.' The calculation method for the pitch is provided by Eq. 2.3, and the parameter setting details for HAYs are presented in Appendix A.2.

2.3.1. Simulation Design

Based on the theoretical model equations(2.1 to 2.16), the main variables for HAYs are identified as diameter ratio and wrap angle (both considered geometric parameters), and Young's Ratio (considered a material parameter). To investigate the impact of these factors on the auxeticity of HAYs, a controlled variable approach was adopted in the simulation experiments.

Firstly, four major groups representing different wrap angles were established: 25°, 30°, 35°and 40°. Within each major group, four subgroups were created based on variations in Young's Ratio: 10, 20, 50 and 100. In these subgroups, the compliant core modulus (E_{CC}) was fixed, with Young's Ratio defined as the ratio of the stiffer wrap modulus (E_{SW}) to the compliant core modulus (E_{CC}).

Within each subgroup, the diameter ratio also varied. With the core diameter (D_{CC}) fixed at 12mm, the sheath diameter (D_{SW}) was varied as 6mm, 4mm, 3mm and 2mm to explore the effects of changing the diameter ratio on the HAYs.

The specific experimental parameters are as follows:

- **Wrap Angle**: 25°, 30°, 35°, 40°
- **Young's Ratio ($\frac{E_{SW}}{E_{CC}}$)**: 100, 200, 500, 1000
- **Diameter Ratio ($\frac{D_{SW}}{D_{CC}}$)**:
  - Fixed $D_{CC}[mm]$ at 12
  - $D_{SW}[mm]$ varied as 6, 4, 3, 2

This design allows for a systematic investigation of the effects of geometric and material parameters on the auxeticity of HAYs, providing a comprehensive understanding. By employing a controlled variable method, the reliability and accuracy of the experimental results are enhanced, as it ensures that when examining the impact of one variable on auxeticity, all other variables remain constant. The completed setting chart is shown in Appendix B.

2.3.2. Abaqus Model Setting

For the building process of finite element analysis model, Y. Ma's method[29] is used. In Abaqus, two parts are created under 'Part': the 'compliant core' fiber and the stiffer wrap fiber. Both parts are defined as three-dimensional, deformable, and solid entities. Due to the varying settings of the models, the elastic modulus and Poisson's ratio, two crucial material properties, are incorporated accordingly.

To accurately model the frictional interaction between the wrapped fiber and the core fiber, a surface-to-surface contact interaction is established between the fiber components. The mechanical constraint is implemented using the kinematic contact method, with tangential behavior defined as the contact action. A friction coefficient of 0.1 is applied to represent the frictional forces between the fibers.

For motion simulation, one end of the fiber is fixed while the other end simulates the tensile motion by applying displacement. At one end, both the compliant core fiber and the stiffer wrap fiber are completely fixed in the initial step (U1 = U2 = U3 = UR1 = UR2 = UR3 = 0) to prevent relative sliding between the two components during stretching. At the opposite end, a reference point, RP-1, is created and coupled to the ends of both the core fiber and wrapped fiber, ensuring they move together during stretching with certain displacement. Additionally, the reference point is constrained in all directions except for the tensile direction, where degrees of freedom are set to 0. The result models are shown in Fig. 2.10.

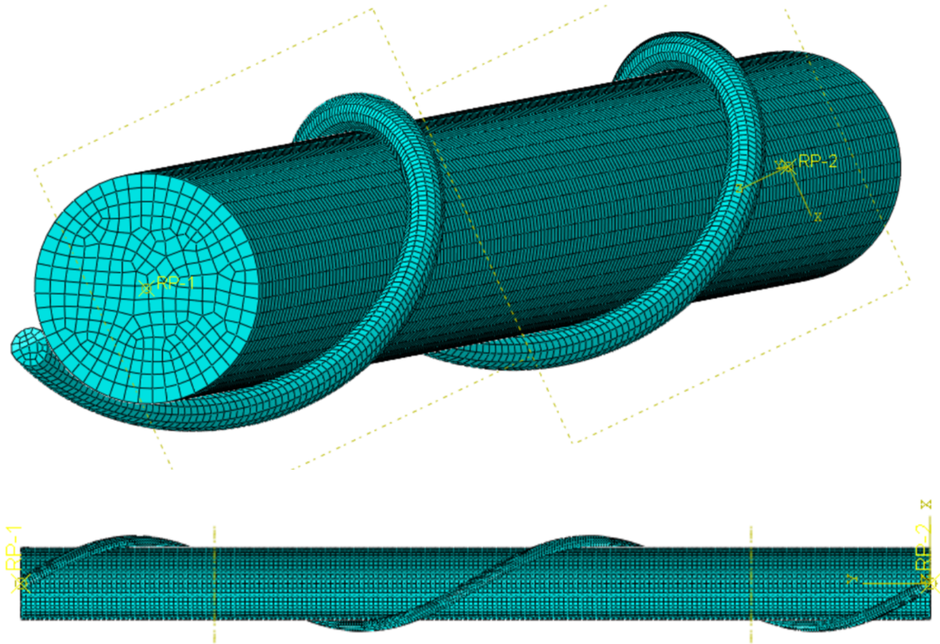

Figure 2.10: Finite element analysis model for stretching

3
Results

3.1. Theoretical Model Representation

This section provides a detailed analysis of the theoretical model developed to represent the behavior of Helical Auxetic Yarns (HAYs) under varying strain conditions. The theoretical model predicts the geometric adjustments and auxetic behavior of HAYs by calculating the relationships between angles, fiber lengths, and effective diameters as the material undergoes axial stretching. Key parameters such as strain and Poisson's ratio are explored to illustrate how HAYs transition from initial to final states, offering a foundational understanding of their auxetic response.

3.1.1. Geometry Parameters Generation Results

The following set of results illustrates the behavior of HAYs under varying strain conditions and the cross sections as predicted by the theoretical model. The Matlab code used to plot the curves can be found in the Appendix A.1.

Fig. 3.1a compares the angles θ and α as functions of axial strain. It reveals that as the strain increases, the angle θ decreases while α increases, indicating a geometric adjustment within the structure.

Fig. 3.1b presents a comparison between the effective diameter D, the compliant core fiber diameter D_C, and the stiffer wrap fiber diameter D_{SW}. The effective diameter D initially decreases and then increases, eventually surpassing its initial value. This behavior satisfies the definition of auxeticity, where the material exhibits an increase in its lateral dimensions when stretched along its axis.

Fig. 3.1c explores the changes in fiber lengths L_{SW} and L_{CC} under strain. While L_{SW} remains constant zero, L_{CC} increases significantly, suggesting that the compliant core fibers undergo substantial elongation relative to the stiffer warp. Finally.

Fig. 3.1d compares the strain experienced by the compliant core (ϵ_{CC}) and the surrounding warp (ϵ_{SW}), which are derived based on eq. 2.17. The strain in stiffer wrap fiber (ϵ_{SW}) is assumed to be constant zero.

In Fig. 3.2, two figures shows the initial state and the final state of HAYs, which contain details like the shape is ellipse in most time and the neutral line of HAYs will shift from the center of Compliant Core fiber to Stiffer Wrap fiber.

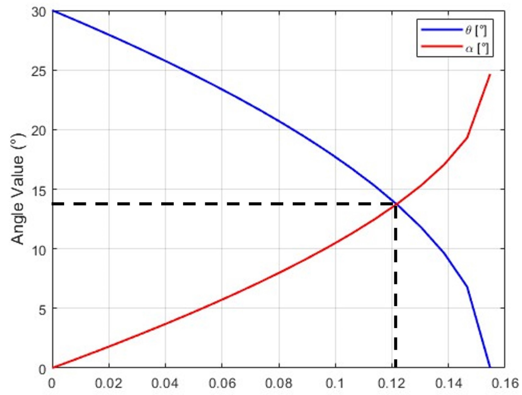

(a) Comparison of θ and α

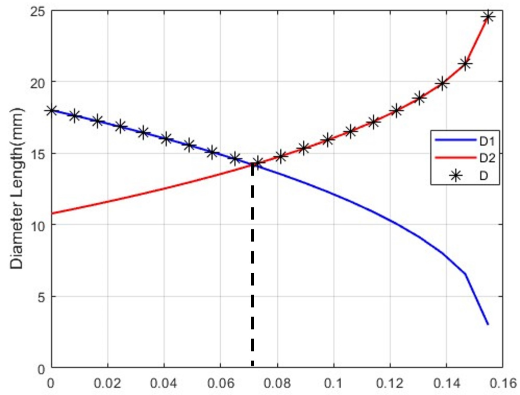

(b) The effective diameter D compare with D_C and D_{SW}

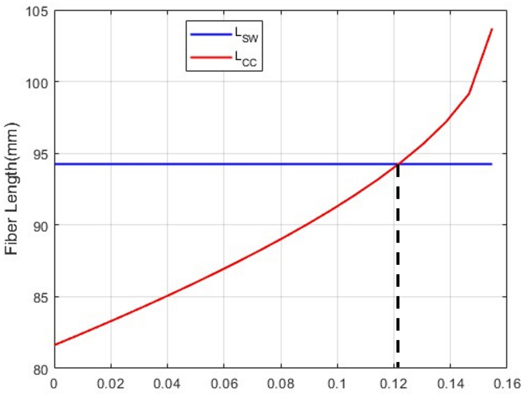

(c) Comparison of L_{CC} and L_{SW}

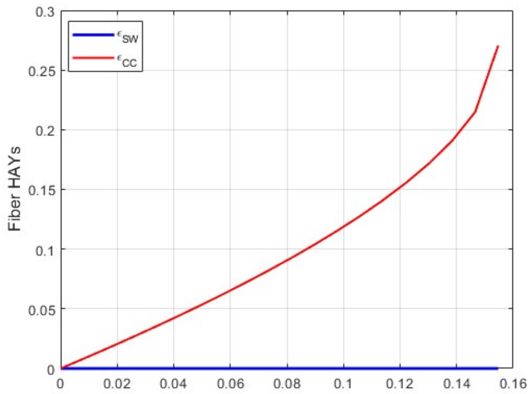

(d) Comparison of ϵ_{CC} and ϵ_{SW}

Figure 3.1: Evolution of (a) The angles of θ and α, (b) The effective diameter of HAYs, (c) The length of the fibers, (d) The strain of both fibers with the change of strain of HAYs

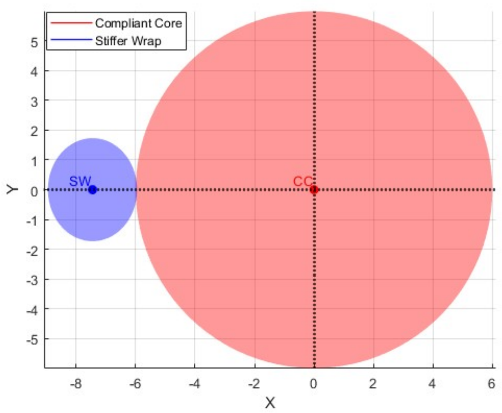

(a) Cross section of HAYs in Initial State

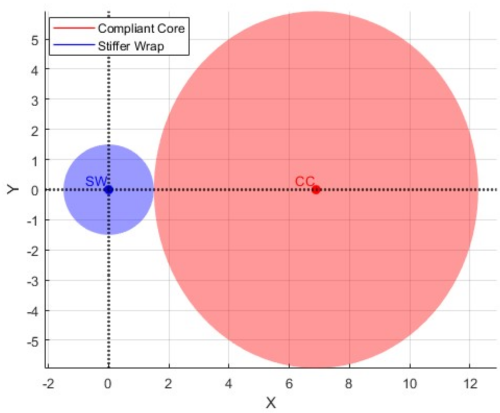

(b) Cross section of HAYs in Final State

Figure 3.2: Cross sections of HAYs in two typical cases: Initial State(a) and Final State(b)

3.1.2. Maple Results

Based on the theory outlined in section 2.1.2, and given the initial geometry parameters such as D_{SW}, D_{CI}, θ, and the material parameters, this work has developed a program in Maple[Appendix A.2] that can generate a 3D visualization of the structural evolution of HAYs under specified conditions. By adjusting the number of states to be displayed, the program allows for the selection of a particular state to showcase the theoretical configuration of HAYs at any given moment. Fig. 3.3 illustrates some significant states which have been analysed in Theoretical Model part.

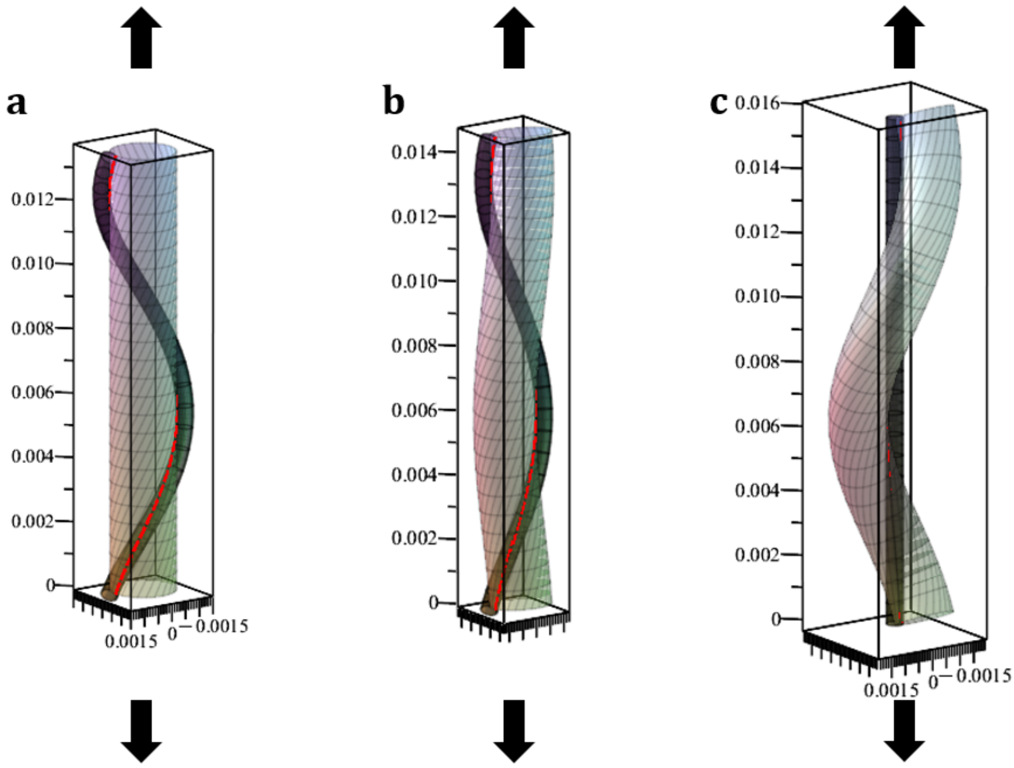

Figure 3.3: Maple results represented the theoretical States of HAYs(Fig. 2.1)

3.2. Abaqus Model Result

In this section, the results of the finite element simulations performed in Abaqus are presented. The simulations illustrate how HAYs respond to tensile deformation, focusing on stress distribution and the interaction between the core and wrap fibers. The section highlights the observation of the engulfment effect and its impact on the material's performance, showcasing how the finite element analysis supports the theoretical predictions of the contact mechanics and stress concentrations within the fibers.

Fig. 3.4 presents several screenshots from an Abaqus finite element simulation, illustrating the stress distribution in HAYs undergoing deformation due to applied displacements at one end.

Fig. 3.5 display the contact pressure on stiffer wrap fiber and compliant core fiber, respectively. It is evident that the maximum compressive stress occurs along the contact line between the two fibers, shown in Fig. 3.5(a)(b). And Fig. 3.5(c) shows a cross-sectional view of the HAYs. It is observed that the mesh for compliant core fiber exhibits a noticeable indentation in the contact region, while the stiffer wrap fiber mesh shows no significant change. This suggests the occurrence of an engulfment effect. Additionally, the maximum stress concentration is also located at the contact point in the cross-section. Overall, these results are close to the theoretical model in Fig. 2.9(c).

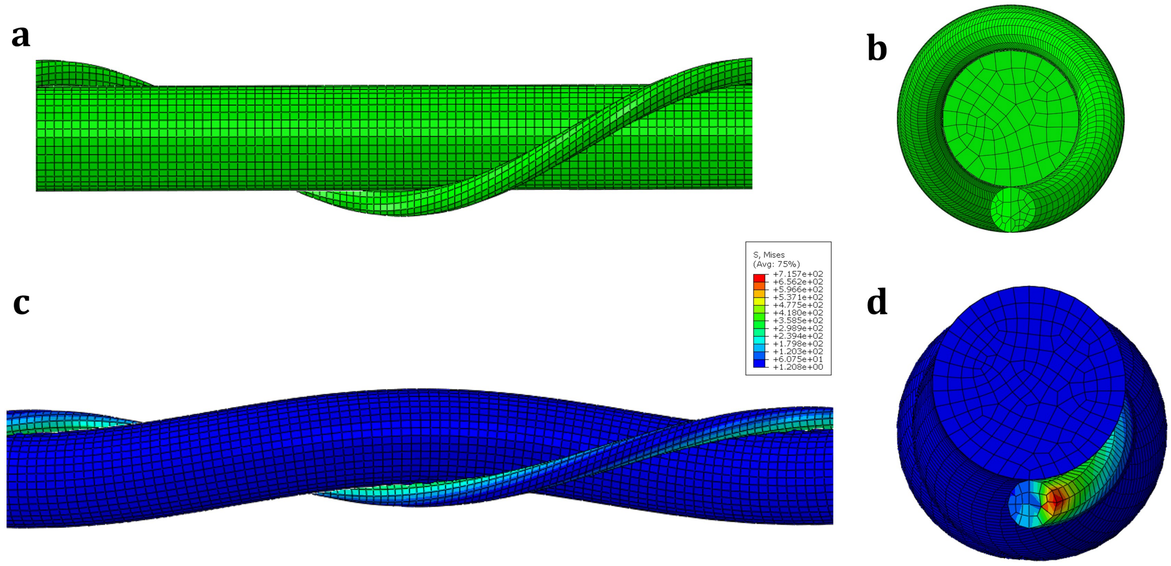

Figure 3.4: The finite element model of HAYs: (a)the model before stretching, (b)the cross section of model before stretching, (c)the model after stretching, (d) the cross section of model after stretching

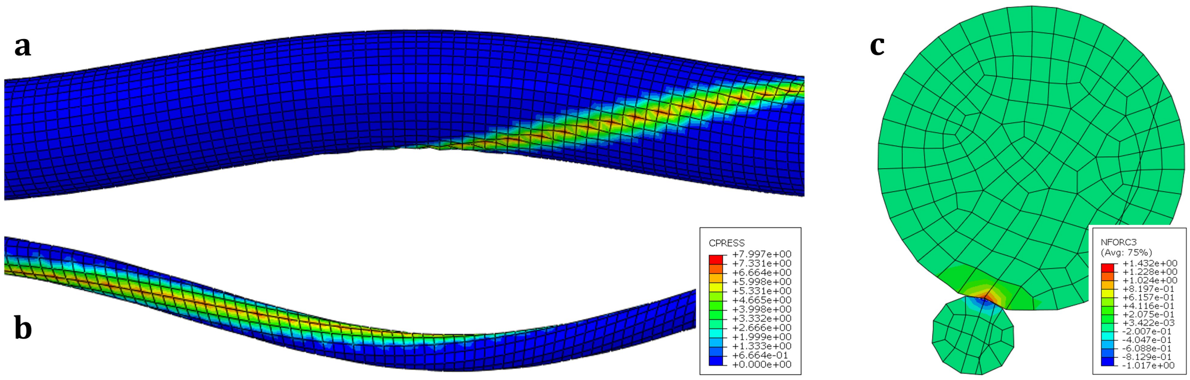

Figure 3.5: Contact loads distribution: (a)(b) maximum stress along the contact line of stiffer wrap and compliant core fibers, (c) mesh deformation and stress concentration in the HAYs cross-section, indicating the engulfment effect

3.3. Comparison of Models with Simulation Results

This section compares the predictions of the theoretical contact models with the results obtained from finite element simulations. The comparison assesses the accuracy and limitations of each model in representing the real-world behavior of HAYs under different strain conditions. Emphasis is placed on the differences in contact pressure, strain, and deformation patterns, helping to validate the models and refine their applicability to auxetic materials.

In Figure 3.6, it shows the comparison between prediction of three contact models(Section 2.2.3) and the results of Abaqus simulation. And it shows the advantage of model 3 and the following work will use model 3 as the contact model.

In Low Strain Model 3 Works Better: At low strains, Model 3 tends to perform better than the other two models, providing a closer approximation to the simulation results. This suggests that Model 3 may better capture the initial elastic response or early-stage deformation characteristics of the material.

Comparison with Simulation Results:

For most cases (e.g., S25A1, S25B1, etc.), the simulation results show a gradual increase in contact pressure, eventually peaking, which aligns with the models' predictions. However, there are variations in the exact magnitude of the peak pressure. In some cases, such as S25A4 and S25B4, the simulation results exhibit a more gradual or delayed increase in contact pressure compared to the models, suggesting that the models might be overestimating the stiffness or the rate of stress increase in these scenarios.

3.4. Poisson's Ratio predicted with changed parameters

This section examines how changes in key parameters, such as diameter ratios, wrap angles, and Young's modulus, affect the Poisson's ratio of HAYs. By systematically altering these parameters, the study analyzes their influence on auxetic behavior, identifying trends in how different configurations enhance or diminish the negative Poisson's ratio. The results provide valuable insights into the optimal design configurations for maximizing auxetic performance while maintaining stability under various strain levels.

3.4.1. Geometrical parameters influence on Poisson's Ratio

Fig. 3.7 illustrates the relationship between Poisson's ratio (PR) and strain of HAYs for different combinations of diameter ratios and wrap angles in HAYs. For Poisson's Ratio of all parameters sets, they all share a climb at small strain and then start to drop.

Higher Diameter Ratio Leads to Better Auxetic Performance: As observed from the plot, configurations with a higher diameter ratio (e.g., $D_{\text{ratio}} = 6$) tend to show better auxetic performance, as indicated by a more pronounced and sustained negative Poisson's ratio, with minimum PR and largest range with NPR.

Lower Wrap Angle Leads to Better Auxetic Performance but Smaller Working Range of Strain: Configurations with a lower wrap angle (e.g., $\theta = 25°$) show better auxetic performance at the starting stages of strain. This is evident from the fact that these configurations have a more obvious negative Poisson's ratio compared to those with higher wrap angles.

However, the trade-off is that these configurations tend to have a smaller working range of strain. The ideal working range of HAYs stops earliest($\approx 10\%$ for $\theta = 25°$,$\approx 15\%$ for $\theta = 30°$,$\approx 20\%$ for $\theta = 35°$,$\approx 30\%$ for $\theta = 40°$). This indicates that while lower wrap angles enhance auxetic behavior, they also limit the range over which this behavior is effective.

3.4.2. Young's Modulus influence on Poisson's Ratio

Four figures (3.8, 3.9) represent how different combinations of diameter ratios and Young's Ratios affect the Poisson's Ratio at wrap angle at $25°$,$30°$,$35°$ and $40°$.

Fig. 3.8a illustrates the relationship between Poisson's Ratio and HAYs' strain for various Young's Ratio configurations under a 25° wrap angle. In this figure, curves of the same color represent different Young's Ratios while keeping the geometry parameters constant. A few key observations can be made:

Firstly, all curves within the same color family exhibit similar trends, aligning well with theoretical predictions (Fig. 3.7). This confirms that, under consistent geometry, the overall behavior of PR with respect to strain remains similar, regardless of the stiffness of the stiffer wrap fiber. Additionally, as the Young's Ratio increases (indicating a stiffer wrap fiber), the PR values tend to be higher for the same strain level. This suggests that higher stiffness in the stiffer wrap fiber diminishes the auxetic effect, resulting in poorer performance in terms of negative PR. Notably, for diameter ratios of 4 and 6, the configuration with $E_{ratio} = 500$ achieves the best performance, despite not having the lowest Young's Modulus ratio.

Fig. 3.8b illustrates the relationship between PR and HAYs' strain for the 30° wrap angle configurations. As with the 25° wrap angle, the most pronounced auxetic performance is achieved with the largest diameter ratio. However, the auxetic effect is less significant, with PR values reaching around -3.

Fig. 3.9a illustrates the relationship between PR and HAYs' strain for the 35° wrap angle configurations. The auxetic behavior is weak only with PR values around -2 but with a large working range with maximum strain of 25%.

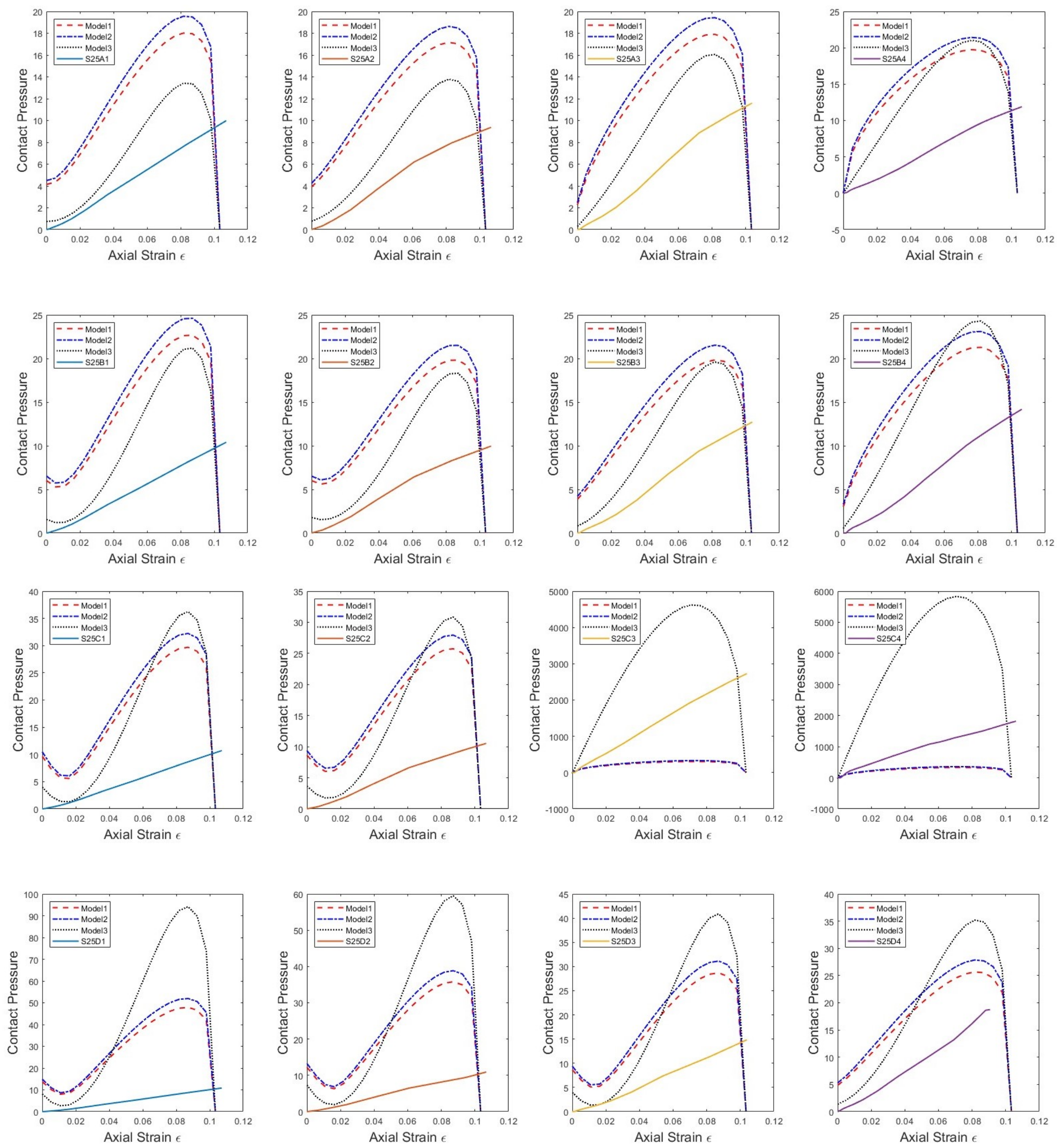

Figure 3.6: Contact Pressure Comparison between three models and the simulation result

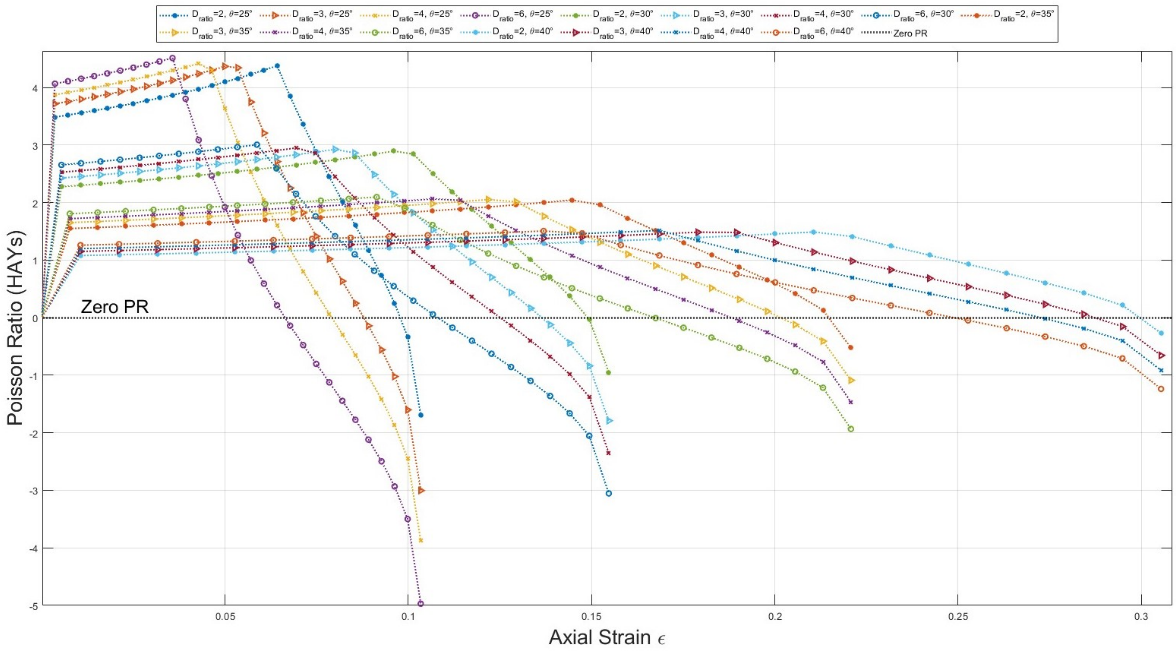

Figure 3.7: Comparison of Poisson's Ratio and Strain of HAYs with combinations of Diameter Ratios and Initial Wrap Angle

Fig. 3.9b illustrates the relationship between PR and HAYs' strain for the 40° wrap angle configurations. The auxetic behavior is weak only with PR values around -2 but with a large working range with maximum strain of 25%

Young's Ratio and Auxetic Performance: Across all wrap angles, a higher Young's Ratio (indicating stiffer wrap fiber) always leads to higher PR values, meaning worse auxetic performance. And the conditions that produce the minimum PR values, and hence the best auxetic performance, are those with the lower Young's Ratios. This suggests that reducing the stiffness of the stiffer wrap fiber, relative to the compliant core fiber, could a key strategy in enhancing the auxetic effect.

Impact of Wrap Angle: Increasing the wrap angle from 25° to 40° appears to generally larger the PR values across all configurations, indicating weaker auxetic behavior. However, the performance is still heavily dependent on maintaining a relative low Young's Ratio.

3.4.3. Comparison with Simulation Results

Four figures (3.10,3.11) represent how different combinations of diameter ratios and Young's Ratios affect the Poisson's Ratio at wrap angle at $25°$,$30°$,$35°$ and $40°$ in the Abaqus simulation. And the comparison between the simulation results and the theoretical predicted results has been carried out.

Initial Peak and Decline: Both the simulation and theoretical models predict a sharp initial rise in Poisson ratio (PR) followed by a decline. However, the peak values and the rate of decline vary, with the theoretical model generally predicting higher peaks.

Trend Consistency: The overall trends are consistent between the two, validating the theoretical model's general applicability. However, discrepancies in exact values and the rate of decline indicate potential differences in assumptions or simplifications within the theoretical model compared to the more detailed simulation.

Negative Poisson Ratio: Both approaches predict that the PR can become negative at higher strains, but the simulation results show more variability in when this occurs and how pronounced the negative values are.

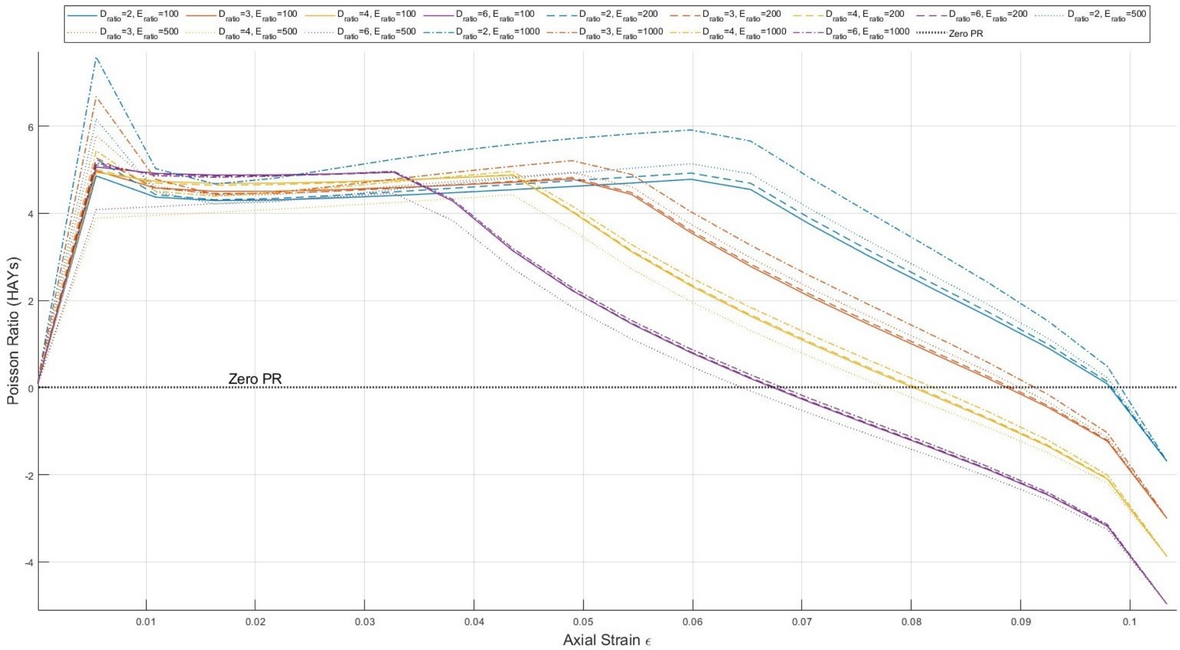

(a) Theoretical results: Comparison of Poisson's Ratio and Strain of HAYs with 25° wrap angle

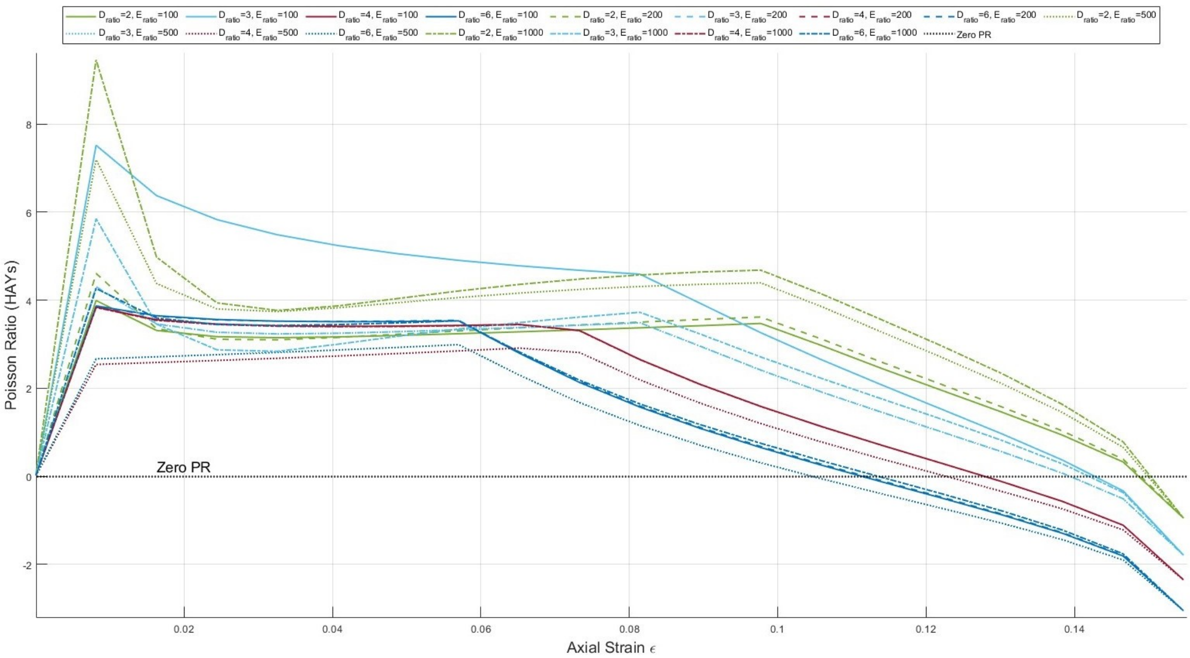

(b) Theoretical results: Comparison of Poisson's Ratio and Strain of HAYs with 30° wrap angle

Figure 3.8: Theoretical results: Comparison of Poisson's Ratio and Strain of HAYs with 25° and 30° wrap angle

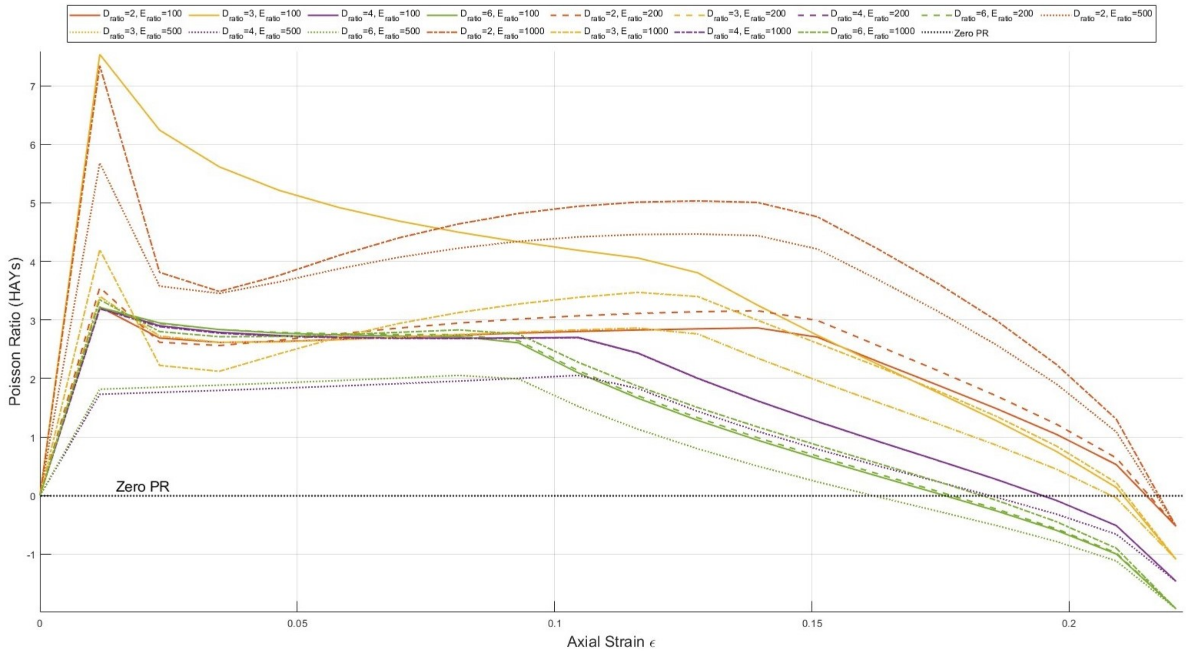

(a) Theoretical results: Comparison of Poisson's Ratio and Strain of HAYs with 35° wrap angle

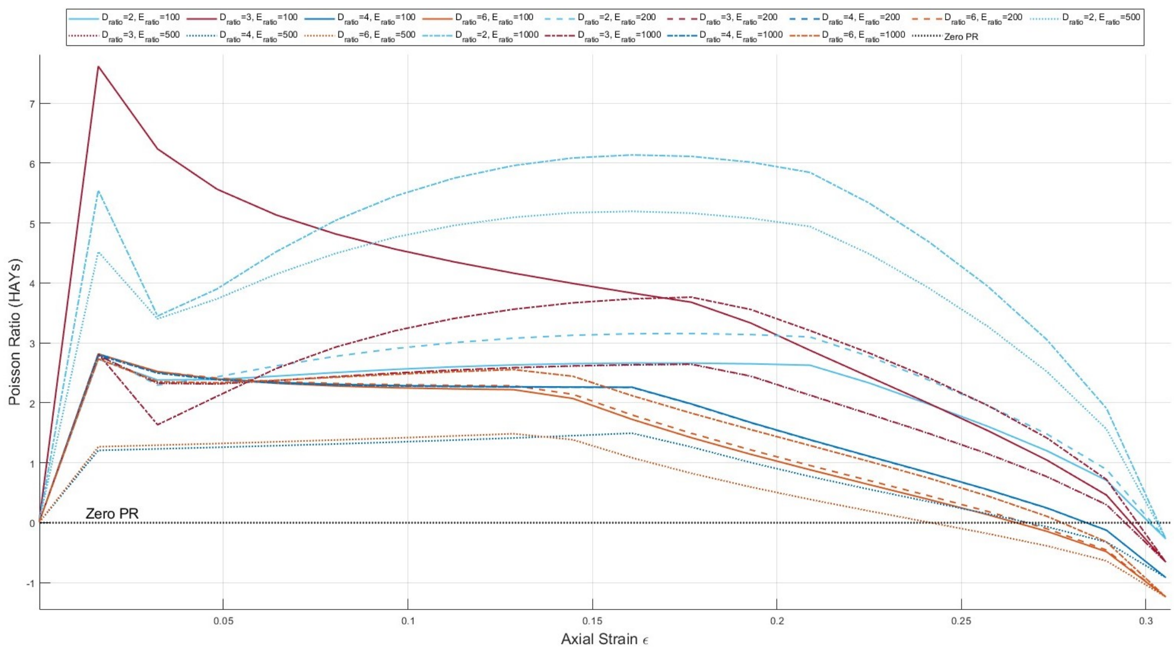

(b) Theoretical results: Comparison of Poisson's Ratio and Strain of HAYs with 40° wrap angle

Figure 3.9: Theoretical results: Comparison of Poisson's Ratio and Strain of HAYs with 35° and 40° wrap angle

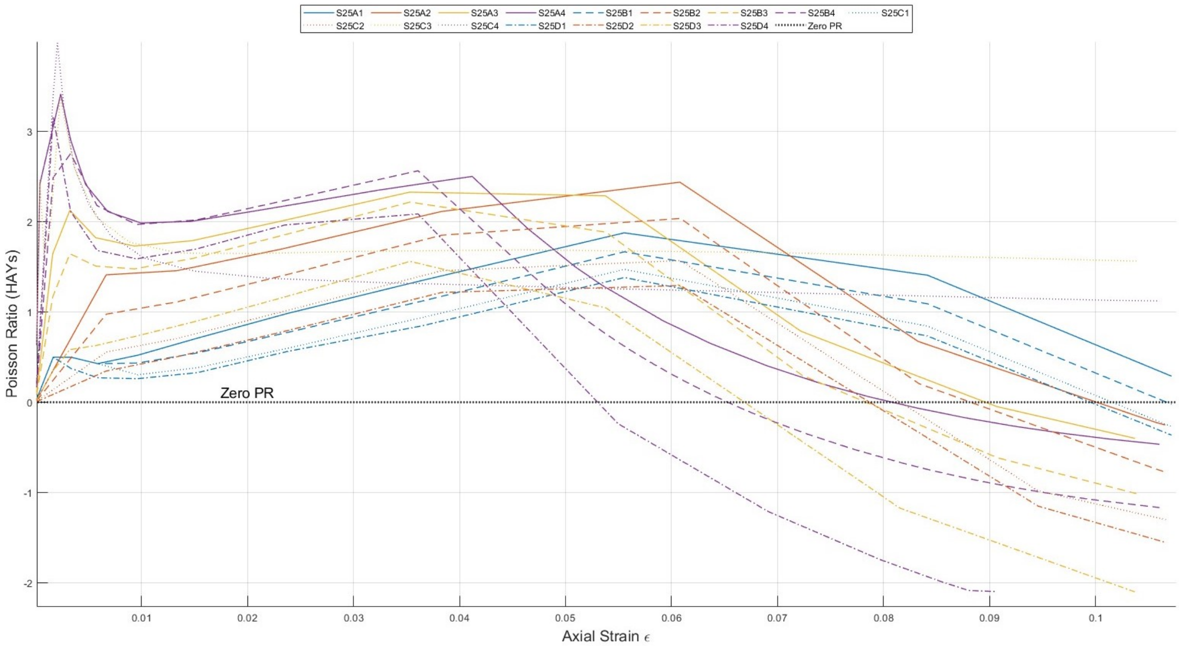

(a) Simulation results: Comparison of Poisson's Ratio and Strain of HAYs with 25° wrap angle

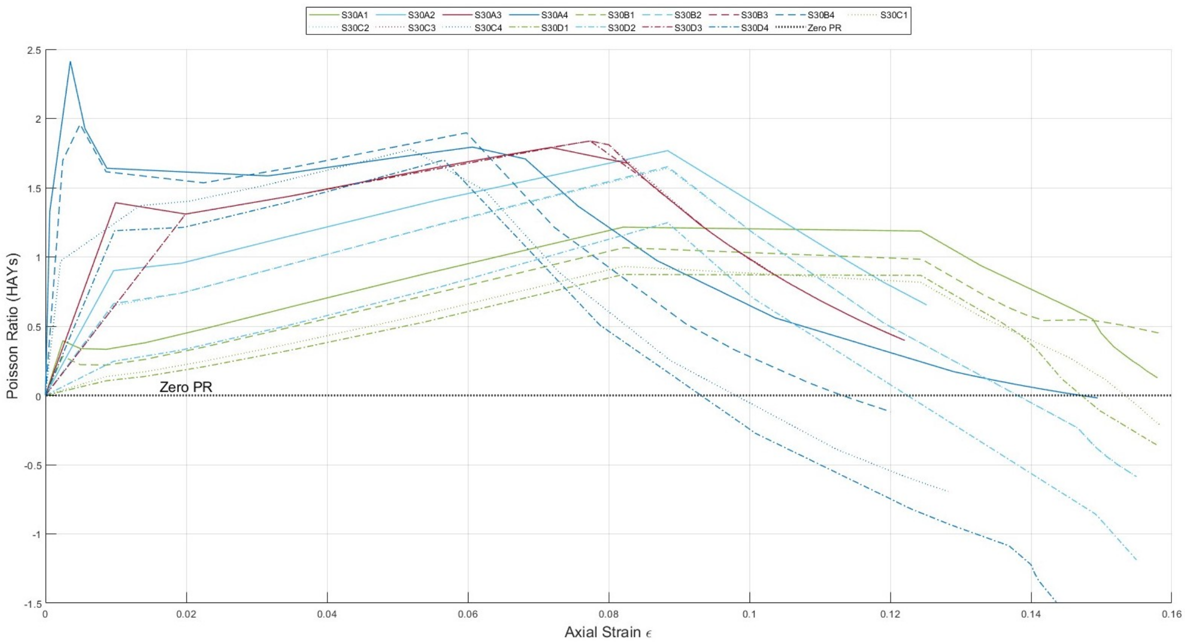

(b) Simulation results: Comparison of Poisson's Ratio and Strain of HAYs with 30° wrap angle

Figure 3.10: Simulation results: Comparison of Poisson's Ratio and Strain of HAYs with 25° and 30° wrap angle

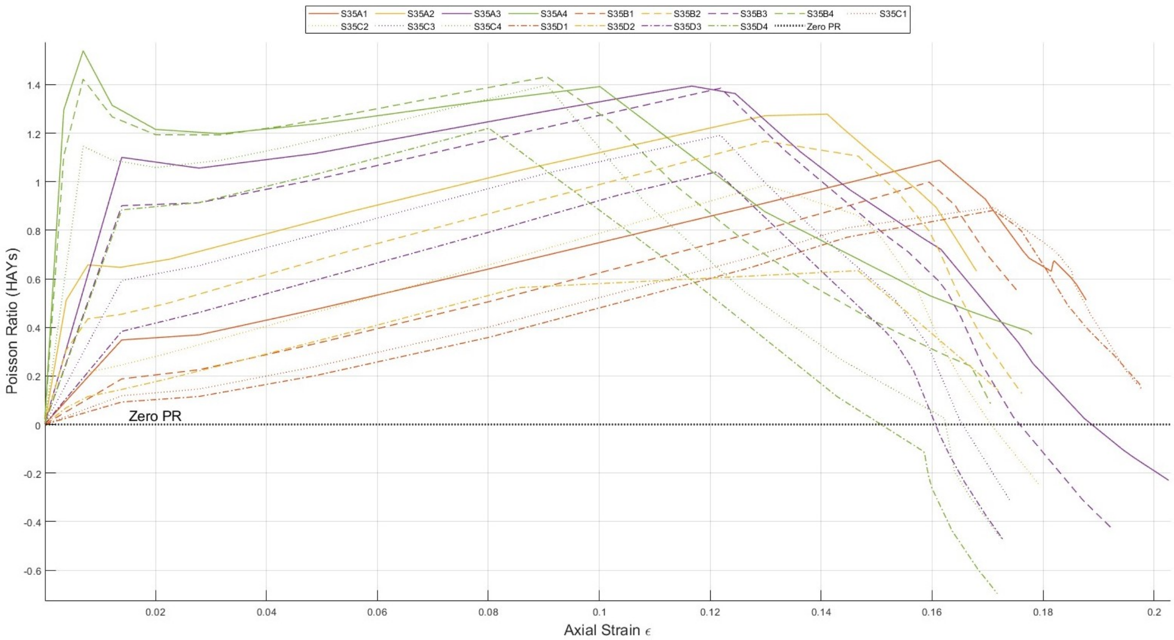

(a) Simulation results: Comparison of Poisson's Ratio and Strain of HAYs with 35° wrap angle

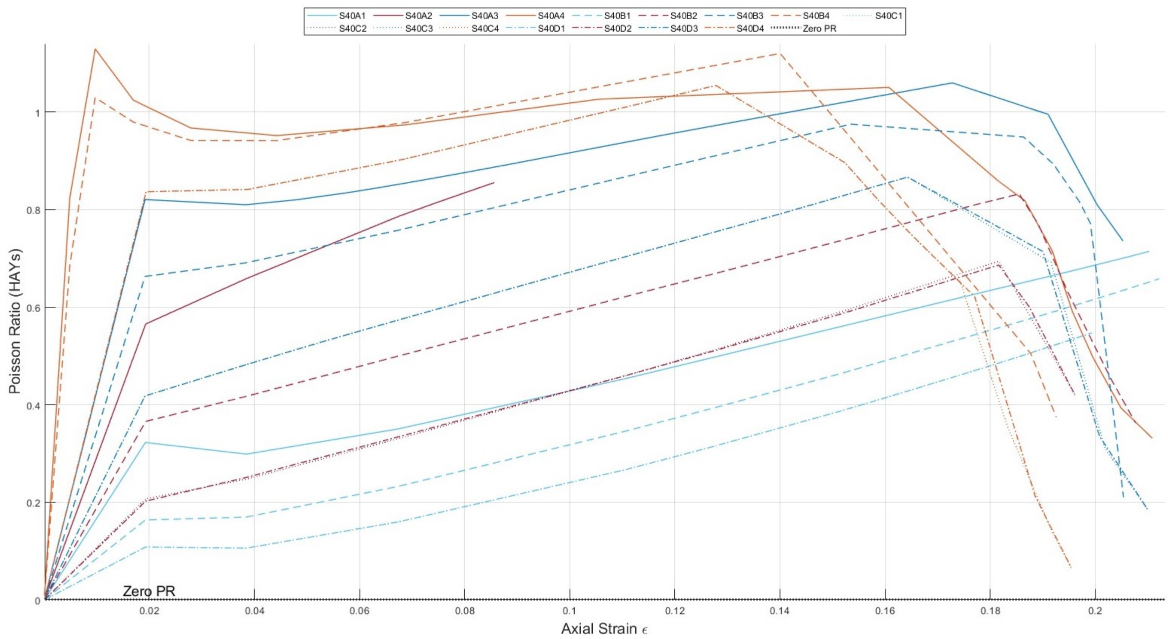

(b) Simulation results: Comparison of Poisson's Ratio and Strain of HAYs with 40° wrap angle

Figure 3.11: Simulation results: Comparison of Poisson's Ratio and Strain of HAYs with 25° and 30° wrap angle

4

Discussion

Ideal and real case of the maximum strain From section 3, in Fig. 3.7, a trade-off between strain range and auxetic behavior is observed. This raises the question of what might occur if the HAYs elongate beyond the maximum strain presented here. According to experimental results from other researchers, shown in Fig. 4.1 , after the initial phase of deformation—where only the compliant core fiber undergoes plastic deformation—both fibers eventually enter a state of plastic deformation. Consequently, the Poisson's ratio value increases as the diameter of the stiffer wrap fiber decreases due to Poisson's effect, which mean HAYs will gradually lose auxeticity after the maximum strain this work discussed.

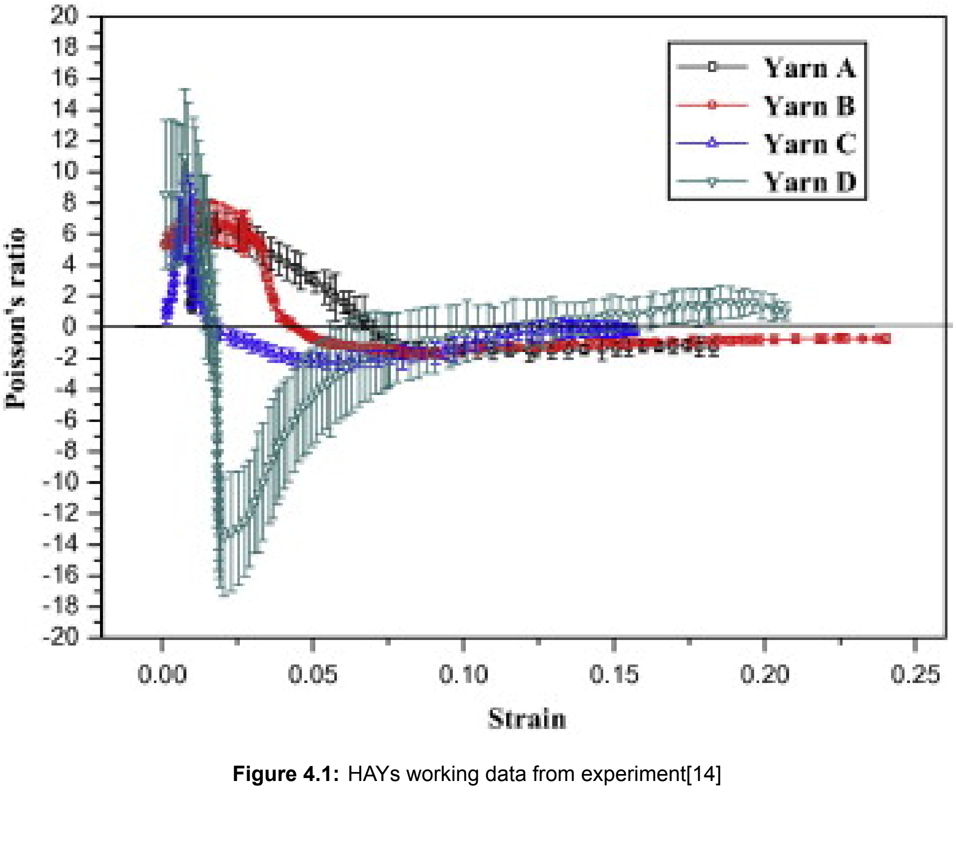

Figure 4.1: HAYs working data from experiment[14]

Suggestions for improving the auxeticity of HAYs The results presented in Section 3 demonstrate that increasing the diameter ratio in the design of HAYs leads to greater lateral expansion when the material is axially stretched. This effect enhances the auxetic behavior, making it an effective strategy for achieving more robust auxetic properties.

However, optimizing the auxetic performance is not solely dependent on the diameter ratio. To mitigate the engulfment effect and further enhance auxetic behavior, it is crucial to focus on reducing the Young's Ratio. This approach consistently results in lower Poisson's ratio values across different configurations. Additionally, while decreasing the wrap angle can amplify auxetic behavior, the most significant improvements are observed when this adjustment is paired with a low Young's Ratio. These insights suggest a clear direction for the design and optimization of auxetic materials, particularly in contexts where auxetic behavior is critical.

Furthermore, both the predictive models and simulation results consistently indicate an initial rise in PR at the beginning of the loading process. To address this issue, one viable approach might be to pre-stretch the HAYs prior to use, effectively bypassing this initial phase of deformation. By doing so, the material could enter its operational phase more quickly, with the auxetic behavior fully engaged from the start. Other methods, such as conditioning the material through cyclic loading or employing a tailored loading protocol, could also be explored to minimize the impact of this initial climb and optimize the performance of HAYs in practical applications.

Performance of Model 3 at Low and High Strains: The results indicate that Model 3 outperforms Models 1 and 2 at low strain levels, providing a closer approximation to the observed behavior. This is likely due to the fact that, at low strains, the deformation remains small and within the elastic range, where the simplified assumptions of Model 3—such as a basic contact model—are sufficient to capture the material's response. However, as the strain increases and the material undergoes larger deformations, the limitations of Model 3 become more apparent. The simple contact model used in Model 3 fails to account for more complex interactions and non-linearities that arise under higher strains, leading to a divergence from the actual behavior observed in the simulations.

Limitations of Model 3 in Representing HAYs: Despite its initial accuracy at low strains, Model 3 still exhibits significant limitations in accurately representing the behavior of real HAYs. One key assumption in Model 3 is that the two fibers lie in parallel planes, which simplifies the contact mechanics. However, in reality, the stiffer wrap fiber is twisted around the compliant core fiber, creating a more complex geometry that involves torque and curvature along the contact length. This twisting introduces additional forces and interactions that are not captured by the parallel plane assumption in Model 3. To better model the true behavior of HAYs, it may be necessary to incorporate these factors, such as the effect of twisting on torque and the impact of curvature on contact mechanics, into the model. This would likely improve the accuracy of predictions across a wider range of strain levels.

Suggestion for experimental validation for future work Despite the theoretical advancements and valuable conclusions drawn from comparing the theoretical predictions with simulation results in this work, there remains a significant gap due to the absence of experimental validation. While the theoretical models and simulations have provided insights and confirmed some innovative concepts, the lack of physical experiments prevents a complete validation of the findings. Conducting experiments with actual HAYs materials would close the loop between theory, simulation, and real-world behavior, providing a more comprehensive understanding and ensuring that the theoretical innovations can be reliably applied in practical applications. Future work should prioritize experimental studies to fully validate and refine the models presented here.

Overall, the work underscore the importance of carefully considering multiple factors in the design of HAYs. By balancing diameter ratio, Young's Ratio, and wrap angle, it is possible to optimize auxetic performance while minimizing unwanted effects such as engulfment. The insights gained from this work provide a valuable foundation for the continued development and refinement of auxetic meta-material.

5 Conclusion

The analysis presented in this work confirms that optimizing the diameter ratio and wrap angle is crucial for tailoring the auxetic properties of HAYs. A higher diameter ratio enhances the auxetic effect, making the material more responsive to axial strain with sustained lateral expansion. Conversely, a lower wrap angle improves the initial auxetic response but limits the range of strain over which this response is maintained. These insights are critical for designing materials with desired mechanical properties, particularly in applications requiring specific auxetic behavior within a defined range of strain.

Model 3, introduced in this work, generally provides a reasonable approximation of the contact pressure behavior as a function of axial strain, especially at low strains. However, as strain increases, the limitations of Model 3 become apparent due to its simplified assumptions. The discrepancies observed between the theoretical models and simulation results suggest that further refinement or calibration might be needed to improve their accuracy, particularly in predicting the exact magnitude of contact pressure under different loading conditions.

Overall, this work contributes valuable insights into the design of auxetic materials, offering guidelines for optimizing HAYs' performance while minimizing adverse effects like engulfment. Future work should include experimental validation to fully bridge the gap between theory, simulation, and real-world application, ensuring that the theoretical advancements can be reliably applied in practice.

References

[1] Wei Yang et al. “Review on auxetic materials”. In: *Journal of materials science* 39 (2004), pp. 3269–3279.

[2] KL Alderson, A Alderson, and KE Evans. “The interpretation of the strain-dependent Poisson’s ratio in auxetic polyethylene”. In: *The Journal of Strain Analysis for Engineering Design* 32.3 (1997), pp. 201–212.

[3] A Alderson and K L Alderson. “Auxetic materials”. In: *Proceedings of the Institution of Mechanical Engineers, Part G: Journal of Aerospace Engineering* 221.4 (Apr. 1, 2007), pp. 565–575. ISSN: 0954-4100, 2041-3025. DOI: 10.1243/09544100JAERO185. URL: http://journals.sagepub.com/doi/10.1243/09544100JAERO185 (visited on 08/25/2023).

[4] L. Ai and X.-L. Gao. “Metamaterials with negative Poisson’s ratio and non-positive thermal expansion”. In: *Composite Structures* 162 (Feb. 2017), pp. 70–84. ISSN: 02638223. DOI: 10.1016/j.compstruct.2016.11.056. URL: https://linkinghub.elsevier.com/retrieve/pii/S0263822316316038 (visited on 12/02/2023).

[5] Yunan Prawoto. “Seeing auxetic materials from the mechanics point of view: a structural review on the negative Poisson’s ratio”. In: *Computational Materials Science* 58 (2012), pp. 140–153.

[6] Andrew Alderson. “A triumph of lateral thought”. In: *Chemistry & Industry* 17 (1999), pp. 384–391.

[7] H. M. A. Kolken and A. A. Zadpoor. “Auxetic mechanical metamaterials”. In: *RSC Advances* 7.9 (2017), pp. 5111–5129. ISSN: 2046-2069. DOI: 10.1039/C6RA27333E. URL: http://xlink.rsc.org/?DOI=C6RA27333E (visited on 08/21/2023).

[8] Arnaud Lazarus and Pedro M Reis. “Soft actuation of structured cylinders through auxetic behavior”. In: *Advanced Engineering Materials* 17.6 (2015), pp. 815–820.

[9] Fabrizio Scarpa. “Auxetic materials for bioprostheses [In the Spotlight]”. In: *IEEE Signal Processing Magazine* 25.5 (2008), pp. 128–126.

[10] Yichao Tang and Jie Yin. “Design of cut unit geometry in hierarchical kirigami-based auxetic metamaterials for high stretchability and compressibility”. In: *Extreme Mechanics Letters* 12 (2017), pp. 77–85.

[11] Tyler J. Cuthbert et al. “HACS: Helical Auxetic Yarn Capacitive Strain Sensors with Sensitivity Beyond the Theoretical Limit”. In: *Advanced Materials* 35.10 (Mar. 2023), p. 2209321. ISSN: 0935-9648, 1521-4095. DOI: 10.1002/adma.202209321. URL: https://onlinelibrary.wiley.com/doi/10.1002/adma.202209321 (visited on 08/26/2023).

[12] Patrick Hook and Auxetix Limited. “(54) USES OF AUXETIC FIBRES”. In: ().

[13] M.R. Sloan, J.R. Wright, and K.E. Evans. “The helical auxetic yarn – A novel structure for composites and textiles; geometry, manufacture and mechanical properties”. In: *Mechanics of Materials* 43.9 (Sept. 2011), pp. 476–486. ISSN: 01676636. DOI: 10/cb7vn3. URL: https://linkinghub.elsevier.com/retrieve/pii/S0167663611000913 (visited on 08/25/2023).

[14] S. Bhattacharya et al. “The variation in Poisson’s ratio caused by interactions between core and wrap in helical composite auxetic yarns”. In: *Composites Science and Technology* 102 (Oct. 2014), pp. 87–93. ISSN: 02663538. DOI: 10.1016/j.compscitech.2014.07.023. URL: https://linkinghub.elsevier.com/retrieve/pii/S0266353814002656 (visited on 12/18/2023).

[15] Zhaoyang Ge, Hong Hu, and Shirui Liu. “A novel plied yarn structure with negative Poisson’s ratio”. In: *The Journal of The Textile Institute* 107.5 (May 3, 2016), pp. 578–588. ISSN: 0040-5000, 1754-2340. DOI: 10.1080/00405000.2015.1049069. URL: http://www.tandfonline.com/doi/full/10.1080/00405000.2015.1049069 (visited on 08/26/2023).

[16] PB Hook. “Composite fibre and related detection system”. In: *US Patent No. US20090193906 A12009* (2009).

[17] W Miller et al. “The manufacture and characterisation of a novel, low modulus, negative Poisson’s ratio composite”. In: *Composites Science and Technology* 69.5 (2009), pp. 651–655.

[18] W Miller et al. “A negative Poisson’s ratio carbon fibre composite using a negative Poisson’s ratio yarn reinforcement”. In: *Composites Science and Technology* 72.7 (2012), pp. 761–766.

[19] JR Wright, MR Sloan, and KE Evans. “Tensile properties of helical auxetic structures: A numerical study”. In: *Journal of Applied Physics* 108.4 (2010).

[20] Julian R Wright et al. “On the design and characterisation of low-stiffness auxetic yarns and fabrics”. In: *Textile Research Journal* 82.7 (2012), pp. 645–654.

[21] KL Alderson et al. “Auxetic polypropylene fibres: Part 1-Manufacture and characterisation”. In: *Plastics, rubber and composites* 31.8 (2002), pp. 344–349.

[22] N Ravirala et al. “Expanding the range of auxetic polymeric products using a novel melt-spinning route”. In: *physica status solidi (b)* 242.3 (2005), pp. 653–664.

[23] Samuel C Ugbolue et al. “The formation and performance of auxetic textiles. Part I: theoretical and technical considerations”. In: *the Journal of the Textile Institute* 101.7 (2010), pp. 660–667.

[24] Julian R Wright et al. “On the design and characterisation of low-stiffness auxetic yarns and fabrics”. In: *Textile Research Journal* 82.7 (May 2012), pp. 645–654. ISSN: 0040-5175, 1746-7748. DOI: `10.1177/0040517512436824`. URL: `http://journals.sagepub.com/doi/10.1177/0040517512436824` (visited on 12/18/2023).

[25] M.E.R. Shanahan and N. Piccirelli. “Elastic behaviour of a stretched woven cloth”. In: *Composites Part A: Applied Science and Manufacturing* 39.6 (June 2008), pp. 1059–1064. ISSN: 1359835X. DOI: `10.1016/j.compositesa.2008.02.012`. URL: `https://linkinghub.elsevier.com/retrieve/pii/S1359835X08000419` (visited on 12/18/2023).

[26] Valentin L. Popov, Markus Heß, and Emanuel Willert. *Handbook of Contact Mechanics: Exact Solutions of Axisymmetric Contact Problems*. Berlin, Heidelberg: Springer Berlin Heidelberg, 2019. ISBN: 978-3-662-58708-9 978-3-662-58709-6. DOI: `10.1007/978-3-662-58709-6`. URL: `http://link.springer.com/10.1007/978-3-662-58709-6` (visited on 03/11/2024).

[27] S Machida and AJ Durelli. “Response of a strand to axial and torsional displacements”. In: *Journal of Mechanical Engineering Science* 15.4 (1973), pp. 241–251.

[28] SK Batra. “17—The normal force between twisted filaments. Part I: the fibre-wound-on-cylinder model—analytical treatment”. In: *Journal of the Textile Institute* 64.4 (1973), pp. 209–222.

[29] Yanxuan Ma et al. “Tensile experiment and numerical simulation of carbon fiber and polyvinyl alcohol fiber helical auxetic yarns”. In: *Fibers and Polymers* 24.8 (2023), pp. 2951–2965.

A

Reference Code

A.1. Matlab code

```
"""
Take initial wrap angle 30° for example, the code show how to calculate all geometry
    parameters along every state. Also, could be used to carried out plots.
"""

theta_initial_degrees = 30;
theta_initial = deg2rad(theta_initial_degrees);

colors = lines(16);

% Pre-allocate storage for results
all_strain_axial = [];
all_PR_HAYs = [];
all_PR_ideals = [];
legends = {};

labels = ["A", "B", "C", "D"];
lineStyles = {'-', '--', ':', '-.'};
markerStyles = {'x', '<', '*','o'};

% Loop through all combinations of Dsw, Esw, and polynomial coefficients
figure(1); hold on;
for k = 1:length(p30_values)
    p = p30_values(k, :);
    set_number = mod(k-1, length(D_ratios)) + 1;
    label_number = 1 + floor((k-1) / length(D_ratios));
    D_ratio = D_ratios(set_number); % Cycles through D_ratios
    Youngs_ratio = Youngs_ratios(label_number); % Cycles through Youngs_ratios
    Dsw = Dc_initial / D_ratio;
    Esw = Ec * Youngs_ratio;

    % Initial State
    dis_SW_initial = Dsw / 2 + Dc_initial / 2;
    Lsw = 2 * pi * dis_SW_initial / sin(theta_initial);
    Lc_initial = Lsw * cos(theta_initial);
    LS_inital = Lc_initial;

    % Final State
    LS_final = Lsw;
    epsilon_max = (LS_final - LS_inital) / LS_inital;

    number_points = 20;
    step_strain = epsilon_max / (number_points - 1);
    strain_axial = 0:step_strain:epsilon_max;

    theta_t = acos((1 + strain_axial) .* cos(theta_initial));
    theta_t_degree = rad2deg(theta_t);
```

```matlab

    LS_t = (1 + strain_axial) .* LS_inital;
    dis_SW_t = Lsw .* sin(theta_t) / (2 * pi);

    % Initial guess
    x0 = [Lc_initial, Dc_initial];

    % Options
    options = optimoptions('fsolve', 'Display', 'none', 'Algorithm', 'trust-region');

    % Call fsolve
    [x, fval, exitflag] = fsolve(@(x) equations(x, LS_final, Dsw, Dc_initial, Lc_initial, nu_c), x0, options);

    % Parse solution
    Lc_final = x(1);
    Dc_final = x(2);

    % Final State
    alpha_final = acos(LS_final / Lc_final);

    dis_c_t = zeros(size(strain_axial));
    Dc_t = zeros(size(strain_axial));
    strain_c_t = zeros(size(strain_axial));

    for m = 1:length(strain_axial)
        x0 = [0, Dc_initial, 0];
        options = optimoptions('fsolve', 'Display', 'none', 'Algorithm', 'trust-region-dogleg');
        [x, fval, exitflag, output] = fsolve(@(x) myEquations(x, Dsw, Lsw, theta_t(m), Dc_initial, nu_c, Lc_initial, LS_t(m)), x0, options);
        dis_c_t(m) = x(1);
        Dc_t(m) = x(2);
        strain_c_t(m) = x(3);
    end

    LswArray = ones(1, length(LS_t)) * Lsw;
    DswArray = ones(1, length(LS_t)) * Dsw;
    Lc_t = (1 + strain_c_t) .* Lc_initial;
    alpha_t = acos(LS_t ./ Lc_t);
    alpha_t_degree = rad2deg(alpha_t);

    a_sw = ones(1, length(theta_t)) * Dsw / 2;
    b_sw = Dsw ./ (2 * cos(theta_t));
    a_cc = Dc_t / 2;
    b_cc = Dc_t ./ (2 * cos(alpha_t));

    beta_t = alpha_t + theta_t;
    beta_t_degree = rad2deg(beta_t);

    delta_l = DswArray .* sin(theta_t);

    R_cur_sw = b_sw .^ 2 ./ a_sw;
    R_cur_cc = b_cc .^ 2 ./ a_cc;
    cur_sw = 1 ./ R_cur_sw;
    cur_cc = 1 ./ R_cur_cc;

    R_eff = 1 ./ (cur_cc + cur_sw);
    E_eff = 1 / ((1 - nu_c ^ 2) / Ec + (1 - nu_sw ^ 2) / Esw);

    cur_engulfment = dis_SW_t ./ (dis_SW_t .^ 2 + (LS_t ./ (2 * pi)) .^ 2);

    T_set = polyval(p, strain_axial);

    T_set_sw = T_set .* cos(theta_t);
    N_Abaqus = T_set_sw .* cur_engulfment;

    delta_depth_M1 = real(1.5 * N_Abaqus ./ E_eff);
    a_1 = sqrt(R_eff .* delta_depth_M1);
    P1 = N_Abaqus ./ (2 * a_1);

```

```matlab
    delta_depth_M2 = real(4 / pi * N_Abaqus ./ E_eff);
    a_2 = sqrt(R_eff .* delta_depth_M2);
    P2 = N_Abaqus ./ (2 * a_2);

    gaussian_radii = zeros(1, 20);
    for m = 1:number_points
        gaussian_radii(m) = real(ContactModel(R_cur_cc(m), R_cur_sw(m), beta_t(m)));
    end

    delta_depth_M3 = real((3 / 4 * N_Abaqus .* delta_l ./ (E_eff .* gaussian_radii .^ 0.5)) .^ (2 / 3));
    a_3 = sqrt(R_eff .* delta_depth_M3);
    P3 = N_Abaqus ./ (2 * a_3);

    dis_c_t = Dsw / 2 + Dc_t / 2 - dis_SW_t;
    D1 = 2 * (Dsw / 2 + dis_SW_t);
    D2 = 2 * (dis_c_t + Dc_final / 2);
    D = max(D1, D2);

    D1_d = 2 * (Dsw / 2 + dis_SW_t - 2 * delta_depth_M3);
    D2_d = 2 * (dis_c_t + Dc_final / 2 - 2 * delta_depth_M3);
    D_d = max(D1_d, D2_d);
    D_initial = Dc_initial + 2 * Dsw;

    PR_ideals = -real(((D - D_initial) / D_initial) ./ strain_axial);

    if k == 11 || k == 12
        PR_HAYs = -real(((D - D_initial) / D_initial) ./ strain_axial);
    else
        PR_HAYs = -real(((D_d - D_initial) / D_initial) ./ strain_axial);
    end
    PR_HAYs(1) = 0;
    engulfment_percentage = real(delta_depth_M3 ./ DswArray * 100);
    error = (D - D_d) ./ D .* 100;

    % Store results for plotting
    all_strain_axial = [all_strain_axial; strain_axial];
    all_PR_HAYs = [all_PR_HAYs; PR_HAYs];
    all_PR_ideals = [all_PR_ideals; PR_ideals];
    legends{end + 1} = sprintf('D_{ratio}=%d, E_{ratio}=%d', D_ratio, Youngs_ratio);

    Set_name = sprintf('S30%s%d', labels{label_number}, set_number);
    ideal_name = sprintf('D_{ratio}=%d, E_{ratio}=%d, without engulfment effect', D_ratio, Youngs_ratio);

     % Plot results for each combination on the same figure
          %theoretical model
%     plot(strain_axial, PR_HAYs, ...
%         'LineStyle',lineStyles(label_number), ...
%         'LineWidth', 1.5, ...
%         'DisplayName',legends{end}, ...
%         'Color', colors(set_number+4, :));
     %simulation results
    plot(data.(Set_name).strain, data.(Set_name).PR, ...
        'LineStyle',lineStyles(label_number), ...
        'LineWidth', 1, ...
        'DisplayName',Set_name, ...
        'Color', colors(set_number+4, :));

%     hold on;
%     plot(data.(Set_name).strain, data.(Set_name).PR, 'LineStyle', lineStyles{subset_number}, 'LineWidth', 1, 'DisplayName', Set_name, 'Color', colors(label_number, :));
%     plot(strain_axial, PR_ideals, 'LineStyle', ":", 'LineWidth', 1, 'DisplayName', ideal_name, 'Color', colors(label_number, :));
%     plot(strain_axial, PR_ideals, 'LineStyle', ":", 'LineWidth', 1.5, 'DisplayName', ideal_name, 'Color', colors(label_number, :));

end
yline(0, ':', 'Color', [0 0 0], 'LineWidth', 2,'DisplayName','Zero PR');
text(0.02, 0, 'Zero PR', 'HorizontalAlignment', 'center', 'VerticalAlignment', 'bottom', 'FontSize', 14, 'Color', [0 0 0]);
```

```
xlabel('Axial Strain \epsilon','FontSize',15);
ylabel('Poisson Ratio (HAYs)','FontSize',15);
% title('Comparison of Poisson Ratio and Axial Strain with 30° wrap angle','FontSize',16);
legend('show', 'Location', 'northoutside', 'Orientation', 'horizontal', 'NumColumns', 9);

grid on;
hold off;

%%
'''
More plots codes for generating theoretical illustration figures.
'''
close all;
figure;
plot(strain_axial, theta_t_degree, 'b-',strain_axial, alpha_t_degree, 'r--');
title('Comparison of theta and alpha');
xlabel('Axial Strain');
ylabel('Angle value');
legend('Theta degree', 'Alpha degree');
grid on;

figure;
plot(strain_c_t,Dc_t);
title('Comparison of Diameter(Compliant Core) and Strain(Compliant Core)');
xlabel('Strain of Compliant Core');
ylabel('Diameter of Compliant Core');
grid on;

figure;
plot(strain_axial,strain_c_t);
title('Comparison of Strain(Compliant Core) and Axial Strain');
xlabel('Axial strain');
ylabel('Strain of Compliant Core');
grid on;


figure;
plot(strain_axial, LswArray, 'b-',strain_axial, Lc_t, 'r--');
title('The Length of the fibers');
xlabel('Axial Strain');
ylabel('Length');
legend('Stiffer Wrap', 'Compliant Core');
grid on;

% figure;
% plot(strain_axial,T_axial_t);
% title('Comparison of Axial tension and Axial Strain');
% xlabel('Axial strain');
% ylabel('Axial tension');
% grid on;
```

A.2. Maple code

Input parameters:

$SW\_diameter := \frac{6}{1000};$
$CC\_diameter\_initial := \frac{12}{1000};$
$theta\_initial := \frac{30 \cdot 2 \cdot \mathrm{Pi}}{360};$
$nu\_CC := 0.45;$
$n\_turns := 1;$
$with\ (LinearAlgebra) :$
$with\ (plots) :$
$with\ (plottools) :$
$with\ (ColorTools) :$
$plotsetup\ (default) :$

Initial State:

$distance\_SW\_initial := \frac{SW\_diameter}{2} + \frac{CC\_diameter\_initial}{2} :$
$distance\_CC\_initial := 0 :$
$length\_SW := simplify\left(\frac{2 \cdot \pi \cdot distance\_SW\_initial}{\sin(theta\_initial)}\right);$
$length\_CC\_initial := simplify\ (length\_SW \cdot \cos\ (theta\_initial));$
$length\_HAYs\_initial := length\_CC\_initial :$
$length\_HAYs\_final := length\_SW :$

Random State:

$get\_strain := (l, l_0) \to \frac{(l - l_0)}{l_0};$
$poisson\_strain\_y := (\varepsilon_x, \nu) \to -\left(1 - (1 + \varepsilon_x)^{-\nu}\right);$
$strain_{\max} := get\_strain\ (length\_HAYs\_final, length\_HAYs\_initial);$
$number\_points := 100;$
$step\_strain := \frac{(strain_{\max} - 0)}{number\_points - 1} :$
$strain\_HAYs\_list := [seq\ (i \cdot step\_strain, i = 0..\ (number\_points - 1))] :$
$length\_HAYs := length\_HAYs\_initial \cdot (1 + \varepsilon_x) :$
$length\_HAYs\_list := map\ (s \to subs\ (\varepsilon_x = s, length\_HAYs), strain\_HAYs\_list) :$

The following strain expressions are for the elastic Compliant Core in transverse and axial directions.

$CC\_radial\_strain := get\_strain\ (d_{CC}, CC\_diameter\_initial);$
$CC\_axial\_strain := get\_strain\ (length\_CC, length\_CC\_initial)$
$: CC\_strain := CC\_radial\_strain = poisson\_strain\_y\ (CC\_axial\_strain, nu\_CC) :$
$CC\_diameter := solve\ (CC\_strain, d_{CC}) :$

$\theta_t := \arccos\left((1 + \varepsilon_x) \cdot \cos\ (theta\_initial)\right);$
$theta\_t\_list := evalf\ (map\ (s \to subs\ (\varepsilon_x = s, \theta_t), strain\_HAYs\_list)) :$
$theta\_final := theta\_t\_list\ [-1] :$

$distance\_SW := \frac{length\_SW \cdot \sin(\theta)}{2 \cdot \pi} :$
$distance\_SW\_list := evalf\ (map\ (s \to subs\ (\theta = s, distance\_SW), theta\_t\_list)) :$
$distance\_SW\_final := distance\_SW\_list\ [-1] :$
$distance\_ContactLine := dist\_SW - \frac{SW\_diameter}{2} :$
$distance\_ContactLine\_list := evalf\ (map\ (s \to subs\ (dist\_SW = s, distance\_ContactLine), distance\_SW\_list)) :$

$eq1 := CC\_dia\_final = \left(\frac{len\_CC\_final}{length\_CC\_initial}\right)^{-nu\_CC} \cdot CC\_diameter\_initial :$
$eq2 := len\_CC\_final = \mathrm{sqrt}\left(\left(2 \cdot \pi \cdot \left(\frac{SW\_diameter}{2} + \frac{CC\_dia\_final}{2} - distance\_SW\_final\right)\right)^2 + (length\_HAYs\_final^2)\right) :$
$symbolic\_solution := solve(\{eq1, eq2\}, \{CC\_dia\_final, len\_CC\_final\}) :$
$numeric\_solutions := map(u \to rhs(u), symbolic\_solution) :$
$CC\_diameter\_final := numeric\_solutions[1] :$
$length\_CC\_final := numeric\_solutions[2] :$

$distance\_CC\_final := distance\_CC\_list\ [-1];$

*distance_ContactLine_*$initial$:= *distance_ContactLine_*$list\,[1]$;
*distance_ContactLine_*$final$:= *distance_ContactLine_*$list\,[-1]$;

First, define the equation for a helix in Cartesian (x,y,z) coordinates, parameterized by (t,u). The parameter t ranges from 0 to 2πn, where n is the number of total turns. u ranges from 0 to 2π. Plot an example of a single-turn helix with major radius r_M, minor radius r_m, and pitch p.

$$helix := (t, u, \theta, r_M, r_m, p) \rightarrow$$
$$\Bigg[r_M \cdot \cos(t+\theta) - r_m \cdot \cos(t+\theta) \cdot \cos(u) + \frac{p \cdot r_m \cdot \sin(t+\theta) \cdot \sin(u)}{2 \cdot \pi \cdot \mathrm{sqrt}\left(r_M^2 + \left(\frac{p}{2 \cdot \pi}\right)^2\right)},$$
$$r_M \cdot \sin(t+\theta) - r_m \cdot \sin(t+\theta) \cdot \cos(u) - \frac{p \cdot r_m \cdot \cos(t+\theta) \cdot \sin(u)}{2 \cdot \pi \cdot \mathrm{sqrt}\left(r_M^2 + \left(\frac{p}{2 \cdot \pi}\right)^2\right)},$$
$$\frac{1}{2 \cdot \pi} p \cdot t + \frac{r_M \cdot r_m \cdot \sin(u)}{\mathrm{sqrt}\left(r_M^2 + \left(\frac{p}{2 \cdot \pi}\right)^2\right)}\Bigg];$$

Final State:

SW_plot_final := $plot3d($$helix($$t, u, 0,$ *distance_SW_final*, $\frac{\textit{SW\_diameter}}{2}$, *length_HAYs_final*$),$
$t = 0..2 \cdot$ *n_turns* $\cdot\, \pi, u = 0..2 \cdot \pi, scaling = constrained, transparency = 0.2)$:

CC_plot_final := $plot3d($$helix($$t, u, \pi,$ *distance_CC_final*, $\frac{\textit{CC\_diameter\_final}}{2}$, *length_HAYs_final*$),$
$t = 0..2 \cdot$ *n_turns* $\cdot\, \pi, u = 0..2 \cdot \pi, scaling = constrained, transparency = 0.6)$:

*Contactline_plot_*$final$:= $plot3d($$helix($$t, u, 0,$ *ContactLine_*$final, 0,$ *length_HAYs_final*$),$
$t = 0..2 \cdot$ *n_turns* $\cdot\, \pi, u = 0..2 \cdot \pi, scaling = constrained, color =$ "red", $thickness = 2, style = line$:

Animation generation

*plots_*$list$:=[$seq((display($[
$plot3d($$helix\,(t, u, 0,$ *distance_SW_*$list\,[k]$, *SW_*$diameter/2,$ *length_HAYs_*$list\,[k])$, ...
$t = 0..2 *$ *n_turns* $* \mathrm{Pi}, u = 0..2 * \mathrm{Pi}, scaling = constrained, transparency = 0.2$),
$plot3d($$helix\,(t, u, \pi,$ *distance_CC_*$list\,[k]$, *CC_diameter_*$list\,[k]\,/2,$ *length_HAYs_*$list\,[k])$, ...
$t = 0..2 *$ *n_turns* $* \mathrm{Pi}, u = 0..2 * \mathrm{Pi}, scaling = constrained, transparency = 0.6$),
$plot3d($$helix\,(t, u, 0,$ *distance_ContactLine_*$list\,[k]\,, 0,$ *length_HAYs_*$list\,[k])\,, t = 0..2 *$ *n_turns* $* \mathrm{Pi}, ...$
$u = 0..2{*}\mathrm{Pi}, scaling = constrained, color =$ "red", $thickness = 2, style = line, linestyle = 3$)],scaling=constrained)
,k=1..*number*_points]) :
$animation := display($*plots_*$list, insequence = true$) :

B

Simulation Experiments Settings

Table B.1: Parameter Settings of HAYs Simulation

Model	$Young's Ratio$	E_{SW} **[**MPa**]**	E_{CC} **[**MPa**]**	D_{CC} **[**mm**]**	D_{SW} **[**mm**]**
			Wrap Angle = 25°		
S25A1	100	10000	100	12	6
S25A2	100	10000	100	12	4
S25A3	100	10000	100	12	3
S25A4	100	10000	100	12	2
S25B1	200	20000	100	12	6
S25B2	200	20000	100	12	4
S25B3	200	20000	100	12	3
S25B4	200	20000	100	12	2
S25C1	500	50000	100	12	6
S25C2	500	50000	100	12	4
S25C3	500	50000	100	12	3
S25C4	500	50000	100	12	2
S25D1	1000	100000	100	12	6
S25D2	1000	100000	100	12	4
S25D3	1000	100000	100	12	3
S25D4	1000	100000	100	12	2
			Wrap Angle = 30°		
S30A1	100	10000	100	12	6
S30A2	100	10000	100	12	4
S30A3	100	10000	100	12	3
S30A4	100	10000	100	12	2
S30B1	200	20000	100	12	6
S30B2	200	20000	100	12	4
S30B3	200	20000	100	12	3
S30B4	200	20000	100	12	2
S30C1	500	50000	100	12	6
S30C2	500	50000	100	12	4
S30C3	500	50000	100	12	3
S30C4	500	50000	100	12	2
S30D1	1000	100000	100	12	6
S30D2	1000	100000	100	12	4
S30D3	1000	100000	100	12	3
S30D4	1000	100000	100	12	2
					Continued on next page

Table B.1 – *Continued from previous page*

Model	$Young'sRatio$	E_{SW} **[**MPa**]**	E_{CC} **[**MPa**]**	D_{CC} **[**mm**]**	D_{SW} **[**mm**]**
Wrap Angle = 35°					
S35A1	100	10000	100	12	6
S35A2	100	10000	100	12	4
S35A3	100	10000	100	12	3
S35A4	100	10000	100	12	2
S35B1	200	20000	100	12	6
S35B2	200	20000	100	12	4
S35B3	200	20000	100	12	3
S35B4	200	20000	100	12	2
S35C1	500	50000	100	12	6
S35C2	500	50000	100	12	4
S35C3	500	50000	100	12	3
S35C4	500	50000	100	12	2
S35D1	1000	100000	100	12	6
S35D2	1000	100000	100	12	4
S35D3	1000	100000	100	12	3
S35D4	1000	100000	100	12	2
Wrap Angle = 40°					
S40A1	100	10000	100	12	6
S40A2	100	10000	100	12	4
S40A3	100	10000	100	12	3
S40A4	100	10000	100	12	2
S40B1	200	20000	100	12	6
S40B2	200	20000	100	12	4
S40B3	200	20000	100	12	3
S40B4	200	20000	100	12	2
S40C1	500	50000	100	12	6
S40C2	500	50000	100	12	4
S40C3	500	50000	100	12	3
S40C4	500	50000	100	12	2
S40D1	1000	100000	100	12	6
S40D2	1000	100000	100	12	4
S40D3	1000	100000	100	12	3
S40D4	1000	100000	100	12	2